國立臺灣大學理學院海洋研究所

碩士論文

Institute of Oceanography

College of Science

National Taiwan University

Master Thesis

全球暖化下黑潮的變化與未來推估

Future Projection and Variability of Kuroshio Under
Global Warming

黃偌栩

Jo-Hsu Huang

指導教授: 曾于恒 博士

Advisor: Yu-Heng Tseng Ph.D.

中華民國 112 年 7 月

July, 2023

國立臺灣大學碩士學位論文
口試委員會審定書
MASTER'S THESIS ACCEPTANCE CERTIFICATE
NATIONAL TAIWAN UNIVERSITY

全球暖化下黑潮的變化與未來推估

Future Projection and Variability of Kuroshio Under Global Warming

本論文係 黃偌栩 R10241104 在國立臺灣大學海洋研究所完成之碩士學位論文，於民國 112 年 7 月 25 日承下列考試委員審查通過及口試及格，特此證明。

The undersigned, appointed by the Institute of Oceanography on 25 July 2023 have examined a Master's thesis entitled above presented by Jo-Hsu Huang R10241104 candidate and hereby certify that it is worthy of acceptance.

口試委員 Oral examination committee:

曾于恒

（指導教授 Advisor）

陳世楠　　　許晃雄　　　I-I Lin

系主任/所長 Director: 謝志豪

摘要

黑潮為西北太平洋之西方邊界流，透過其顯著的熱量傳輸以及海氣交互作用，可以對海洋的生態、天氣甚至是氣候造成很大的影響。然而，過去對於其未來暖化情境下的變化，與其背後的主導機制，並沒有明確且一致的結論。有些研究認為，暖化下的聖嬰現象或極區震盪趨勢，可以增強中緯度的反氣旋式風場，使該處的黑潮迴流增強；有些研究則認為暖化的副熱帶模態水，經由大洋環流傳輸到黑潮的東側，使黑潮的斜壓性特徵增強、上層流速增加。

本研究使用 28 個 CMIP6 低解析度模式在 SSP5-8.5 未來暖化情境的模擬進行集合分析。結果顯示整體而言，日本沿岸黑潮的動能與流量皆有增強的趨勢，而東海黑潮則有減弱的現象。此外，東海黑潮的動能變化有上層 300 公尺增強，而下層減弱的斜壓性變化。然而，因為琉球島鏈周圍在上層 300 公尺有反氣旋式的環流變化，使得此處的淨流量並沒有明顯的變化。相較至下，5 個高解析度模式集合顯示，日本沿岸黑潮及黑潮迴流的動能及流量皆有更顯著的增強趨勢，且黑潮延伸流域有往極區移動的情形。此外，東海黑潮在上層為減弱的趨勢，與下層變化相同，表示在高解析度模式中，東海黑潮並沒有顯著的斜壓性變化。本研究也發現不論何處的黑潮，不同模式中的經向傳輸變化與風應力旋度變化皆呈顯著的負相關，且日本沿岸黑潮變化對風應力旋度變化在高解析度模式中更加敏感。進一步的敏感度測試顯示，暖化後的海表溫度主導了北緯 35 度以南的黑潮在上層 300 公尺的變化，而風應力旋度則主導 300 公尺以下的變化。等密面上增暖的海
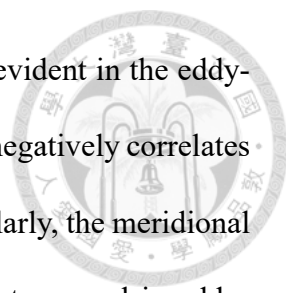
水透過副熱帶模態水傳輸，使黑潮東側的海溫變得更暖，增強了跨黑潮的緯向密度梯度，因此向北的黑潮流速增加。

關鍵字：黑潮、CMIP6、動能、正壓流函數、副熱帶模態水、斜壓性變化

Abstract

Kuroshio plays a critical role in the ocean ecosystem, weather, and even climate in the Western North Pacific through its significant heat transport and air-sea interaction. The future change and dominant mechanism behind it under global warming remain unclear. Some previous studies suggested a negative midlatitude wind stress curl tendency, potentially driven by El Niño or Arctic Oscillation, may accelerate the Kuroshio recirculation. The other studies found that the warmer subtropical mode water might be transported to the east of the Kuroshio along the isopycnals, enhancing the upper-layer velocity under a warmer climate.

Our analysis of the ensemble of 28 CMIP6 low-resolution models in the SSP5-8.5 future scenario projection shows that the kinetic energy and transport tendency of the Kuroshio along Japanese coast (JP-Kuroshio) is positive while the ECS-Kuroshio is negative. Additionally, the kinetic energy of ECS-Kuroshio increases in the upper 300 m and decreases below 300 m (i.e., baroclinic change). However, the transport of it does not change significantly in the upper 300 m because of the anticyclonic circulation change surrounding the Ryukyu Island chain. Compared with the result above, the ensemble of 5 eddy-permitting models shows that the kinetic energy and transport of JP-Kuroshio, including the southern recirculation gyre, enhances more dramatically and the Kuroshio extension moves poleward, while the ECS-Kuroshio decreases in the whole water col-

umn. This suggests the consistent baroclinic increase in ECS is not evident in the eddy-permitting models. We also find that the meridional transport change negatively correlates well with the wind stress curl change across different models. Particularly, the meridional transport change of the JP-Kuroshio is more sensitive to the wind stress curl in eddy-permitting models. Further ocean model experiments suggest that warmer sea surface temperature dominates the Kuroshio change in the upper 300 m to the south of 35°N while the impact of wind stress curl determines the change below 300 m. Warmer isopycnal temperature transport through the subtropical mode water pathway increases the zonal gradient across the Kuroshio and intensify the meridional velocity.

Contents

List of Figures

List of Tables

Chapter 1 Introduction

1.1 The Kuroshio System and its Future Change

Kuroshio, the wind-driven western boundary current in the North Pacific, flows northward from the North Equator Current along the coast of Taiwan. It separates eastward from Japan at around 35°N and forms the Kuroshio Extension (KET), in which high mesoscale eddy activities exist. The southern recirculation gyre (SRG, i.e., Kuroshio recirculation), which flanks south of the KET around 31 to 35°N, can potentially be strengthened by potential vorticity (PV) advection or eddy activities (e.g., Marshall and Nurser, 1986; Jayne et al., 1996; Waterman and Jayne, 2011) and is highly correlated with the KET state (Qiu and Chen, 2005, 2010; Wu et al., 2021). Additionally, in winter and spring, the cold and dry air outbreaks from the nearby continents result in significant surface heat loss from the warm KET region. This heat loss induces deep mixing through convective instability, leading to the formation of a homogeneous and low stratification water mass known as subtropical mode water (STMW). The STMW subducts around the SRG and transports southeast to southwest along subsurface isopycnals propelled by the wind-driven subtropical gyre (Hanawa and Talley, 2001).

The Kuroshio system (Figure 1.1), as a whole, plays a critical role in the ocean ecosystem, weather, and even climate, through its significant heat transport and air-sea interaction (e.g., Small et al., 2008). Thus, it is essential to investigate its potential changes under
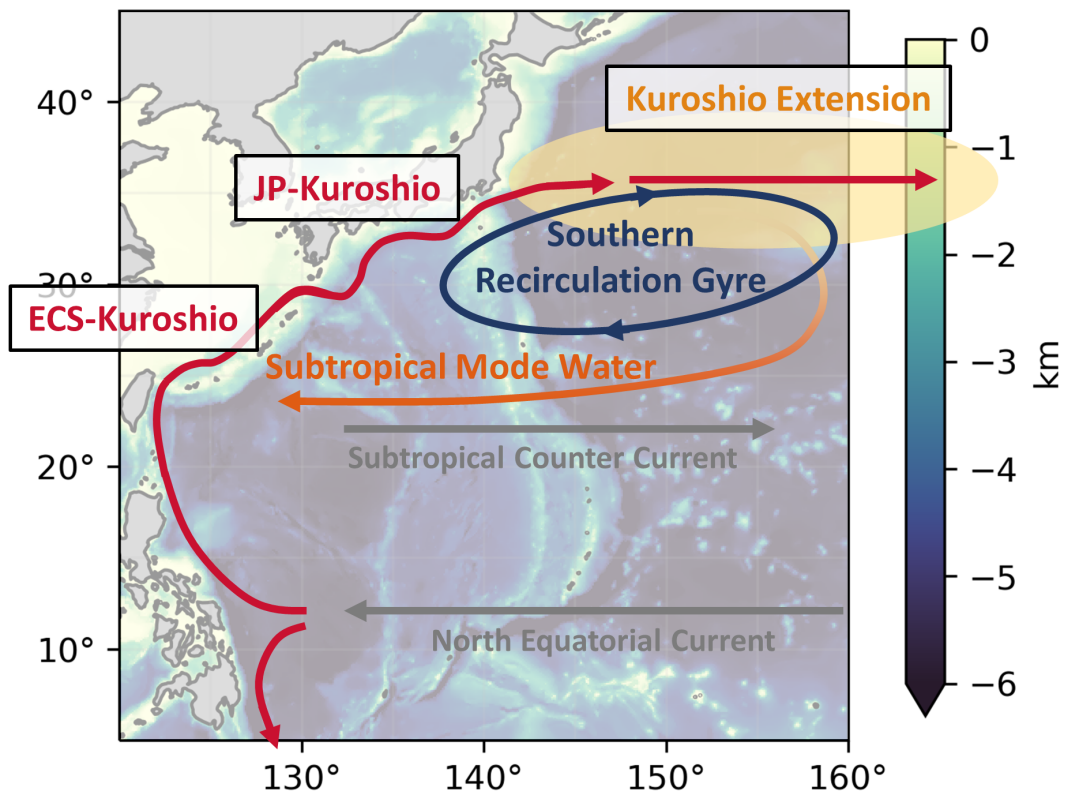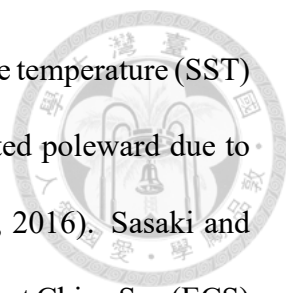
Figure 1.1: Schematic of the Western North Pacific surface currents. The topography is shaded (in km).

global warming. Both the observation and reanalysis data of sea surface temperature (SST) suggested that the Kuroshio has strengthened, and the KET has shifted poleward due to changes in the wind stress curl (WSC) (Wu et al., 2012; Yang et al., 2016). Sasaki and Umeda (2021) also confirmed that the SST warming tendency in the East China Sea (ECS) for over a century had been induced by the accelerated Kuroshio advection. However, it is challenging to identify whether the trend is a consequence of anthropogenic forcing or large-time-scale natural variability due to a lack of long-term observation (Seager et al., 2001; Wang et al., 2016; Yang et al., 2016). Additionally, the velocity changes are inconsistent among these trends (Yang et al., 2016), making model simulation in a warming climate essential.

Furthermore, there is still disagreement about the future changes of Kuroshio and the dominant mechanism based on previous simulations. Some models with a focus on the Kuroshio east of the Japanese coast (JP-Kuroshio) have suggested that a negative midlatitude WSC tendency occurs, potentially driven by a positive El Niño Southern Oscillation (ENSO) or positive Arctic Oscillation (AO)-related signal. These changes cause a poleward shift and intensification of westerlies, resulting in the acceleration of the KET so as to move it poleward associated with a stronger SRG (Sakamoto et al., 2005; Sato et al., 2006; Cheon et al., 2012; Yang et al., 2016; Sen Gupta et al., 2021). However, Yamanaka et al. (2021) showed that these changes are insignificant when examining the Kuroshio net transport along 137°E where the flow begins to turn eastward, and the uncertainty mainly comes from the wide variance of ensemble models. Moreover, based on the Sverdrup theory, Zhang et al. (2017) claimed that not only the wind stress but also the strengthened ocean stratification speed up the JP-Kuroshio through PV conservation to enhance eddy

3

kinetic energy (EKE) in the downstream KET. Peng et al. (2022) also suggested that the stratification enhances the upper subtropical gyre by their idealized experiments.

The future projected Kuroshio change in the ECS (ECS-Kuroshio) is more complicated than that in the JP-Kuroshio. Opposite to the JP-Kuroshio, the overall transport in the ECS-Kuroshio may be decreased by the positive subtropical WSC change (Cheon et al., 2012; Sen Gupta et al., 2021). Nevertheless, studies showed that the speed in the upper layer of Kuroshio may be increased (Chen et al., 2019; Sen Gupta et al., 2021). Using the idealized ocean general circulation model (OGCM) experiments based on CMIP5 RCP4.5 surface warming scenario, Chen et al. (2019) found that the warmer SST may modulate the STMW temperature by vertical mixing, transport to the east of the Kuroshio along isopycnals, and thus enhance the upper-layer velocity by baroclinicity. They suggested that sea surface warming dominates the future change of Kuroshio, including ECS.

1.2 Mesoscale Eddies around the Kuroshio System

Two major eddy-rich regions exist in the western North Pacific: east of Taiwan and the KET, driven by strong, horizontal velocity shear and surface wind. These eddies can profoundly affect the mean current, oceanic front, meridional heat transport, and even atmosphere (e.g., Small et al., 2008; Kida et al., 2016; Chang et al., 2018). However, most of the OGCMs today cannot fully resolve them due to the coarse resolution ($\sim 1° \times 1°$). The lack of mesoscale eddies may potentially relate to the common northward overshoot of Kuroshio separation latitude in these coarse resolution OGCM compared with observation (e.g., Hurlburt et al., 1996; Choi et al., 2002; Qiu et al., 2015), not to mention that the large meander state of Kuroshio along the south Japanese coast can not be fully resolved

4
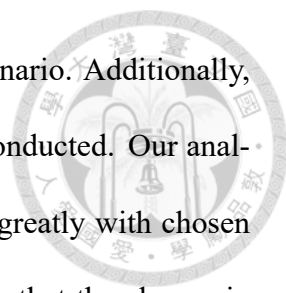
where mesoscale eddies occur extensively (Tseng et al., 2012). Besides, Ma et al. (2016) proposed that the KET mean flow will be less energetic, unstable, and northward without consideration of the feedback between ocean mesoscale eddies and the atmosphere.
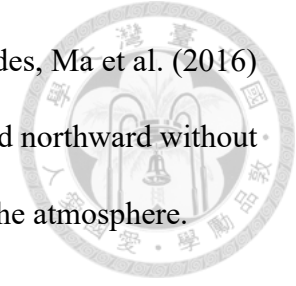
Despite the obstacles above, the observation hints at the eddies change in the past few decades. Hu et al. (2020) inferred that the intensified wind work produced by the negative Pacific decadal oscillation (PDO) phase had dramatically enhanced the upper 2000 m EKE from 1990 to 2013, particularly in tropical region. The sea surface from satellites over 30 years indicates that the EKE in the KET has increased and moved poleward with an insignificant trend, which may be due to large interannual variability and cancellation effect of the poleward shift (regions of EKE increase and decrease cancel out each other in a fixed KET domain defined by climatology; Martínez-Moreno et al., 2021). The difference between these studies is likely caused by the data resolution or ocean dynamics in depths. Again, it is still difficult to observe the effect of global warming with the time restriction and data incompleteness.

1.3 Motivation and Objective of the Study

Although the Kuroshio change under global warming has been widely explored by various products, there is a lack of consensus on the tendency and the underlying causes (Table 1.1). Several studies have focused on the JP-Kuroshio and ECS-Kuroshio separately. Some studies specifically analyze the upper ocean, while others investigate the entire water column. Besides, these studies employ various models and scenarios to simulate warming conditions. Furthermore, the role of the eddies in the Kuroshio change has not been carefully examined. This study aims to investigate the changes and the underlying

physical mechanisms of Kuroshio and KET under future warming scenario. Additionally, a comparative analysis between low and high resolution models is conducted. Our analysis of CMIP6 ensembles shows that the changes of Kuroshio vary greatly with chosen locations and model resolution. Our OGCM sensitivity test suggests that the change in Kuroshio is primarily dominated by surface warming in the upper ocean and WSC beneath.

The rest of this thesis is organized as follows: In chapter 3, the Kuroshio and thermal structure change in the Coupled Model Intercomparison Project phase 6 (CMIP6) future scenario will be analyzed, notably contrasts between coarse (low) and eddy-permitting (high) resolution. In chapter 4, similar to Chen et al. (2019) experiments, an OGCM is driven by future wind field and SST to know whether different OGCM and warming scenarios will reproduce a similar result. Finally, in chapter 5, we compare the difference between each part of the Kuroshio and the different models' simulations above and discuss the mechanism of the Kuroshio system under global warming.

Table 1.1: Summary of the previous studies about Kuroshio change. Note that the trends do not represent the responses to global warming because of the large-time-scale variability for reanalyses data. ”*” indicates eddy-permitting model. ”∼” indicates the trend is not significant. ”/” indicates that the study didn't mention it.

Reference	Data / Model	Trend	KE shift	Cause
Wu et al. 2012	reanalyses	+ (upper)	poleward	wind stress
Yang et al. 2016	reanalyses	+ (upper)	equatorward	wind stress
	CMIP5	+ (upper)	poleward	
Sasaki and Umeda 2021	reanalyses	+ (ECS, upper)	/	wind stress
	*ROMS			
Sakamoto et al. 2005	*MIROCv3.2	+ (JP ,upper)	/	wind stress
Sato et al. 2006	*NPOGCM	+ (JP)	poleward	wind stress
Cheon et al. 2012	CMIP3 *MIROCv3.2	+ (JP)	poleward	wind stress
		- (ECS)		
Zhang et al. 2017	*MIROC4h	+ (JP, upper)	/	stratification
Chen et al. 2019	NEMO OPA	+ (JP)	/	subtropical mode water
		+ (ECS, upper)		
		−(ECS, lower)		
Sen Gupta et al. 2021	CMIP6	+ (JP)	/	wind stress
		∼ (ECS, upper)		
		+ (ECS, lower)		
Yamanaka et al. 2021	*MRI.COMv4	∼ (JP)	poleward	/
Peng et al. 2022	MITgcm	+ (upper)	/	stratification
		−(lower)		

Chapter 2   Methodology

2.1   Coupled Model Intercomparison Project 6 (CMIP6)

In this study, 33 state-of-art CMIP6 models with different spatial resolutions are used (Table 2.1). The most severe warming scenario, SSP5-8.5, is selected for analysis. To adequately resolve mesoscale eddies, a grid size of at least 0.1° is generally required (Delworth et al., 2012; Kirtman et al., 2012). Particularly, even a higher resolution is necessary for the high latitude due to the baroclinic Rossby radius of deformation (Hallberg, 2013). However, most modern OGCMs use coarse resolutions ($\sim 1° \times 1°$), making them impossible to resolve these eddies. Eddy-permitting models have grid sizes between these two extremes and can reasonably simulate incomplete eddy characteristics. Thus, we categorized the CMIP6 models into two groups in our ensemble analysis: low resolution (LR, $\sim 1° \times 1°$) and high resolution (HR, $< 1° \times 1°$), depending on whether the model is eddy-permitting. Note that the Gent-McWilliams parameterization (Gent and Mcwilliams, 1990), which is often used to parameterize mesoscale eddies in coarse resolution models, is not utilized in any HR models in this study, except for MPI-ESM1-2-HR. All data are interpolated to a $0.25° \times 0.25°$ spatial resolution, the highest resolution used in the CMIP6 ocean models, for analysis.

9

Table 2.1: Horizontal nominal resolution (res.) and vertical layers of the CMIP6 models ocean component. Gent-McWilliams (GM) is a parameterization for mixing along isopycnal by mesoscale eddies (Gent and Mcwilliams, 1990).

Model Name	Nominal Res. × Layers	GM	Model Name	Nominal Res. × Layers	GM
ACCESS-CM2	1°× 50	◯	EC-Earth3-CC	1°× 75	◯
ACCESS-ESM1-5	1°× 50	◯	FGOALS-g3	1°× 30	◯
AWI-CM1-1-MR	0.25°× 46	×	FIO-ESM-2-0	1°× 60	◯
BCC-CSM2-MR	1°× 40	◯	GFDL-CM4	0.25° × 75	×
CAMS-CSM1-0	1°× 50	◯	GISS-E2-1-G	1°× 40	◯
CAS-ESM2-0	1°× 30	◯	HadGEM3-GC31-LL	1°× 75	◯
CESM2	1°× 60	◯	HadGEM3-GC31-MM	0.25° × 75	×
CESM2-WACCM	1°× 60	◯	IPSL-CM6A-LR	1°× 75	◯
CIESM	1°× 60	◯	MIROC6	1°× 63	◯
CMCC-CM2-SR5	1°× 50	◯	MIROC-ES2L	1°× 63	◯
CMCC-ESM2	1°× 50	◯	MPI-ESM1-2-HR	0.4°× 40	◯
CNRM-CM6-1	1°× 75	◯	MPI-ESM1-2-LR	1°× 40	◯
CNRM-CM6-1-HR	0.25°× 75	×	MRI-ESM2-0	1°× 61	◯
CNRM-ESM2-1	1°× 75	◯	NESM3	1°× 46	◯
CanESM5	1°× 45	◯	TaiESM1	1°× 60	◯
CanESM5-CanOE	1°× 45	◯	UKESM-0-LL	1°× 75	◯
EC-Earth3	1°× 75	◯	Total: 33, include 5 High Resolution		

2.2 TaIwan Multi-scale Community Ocean Model (TIMCOM)
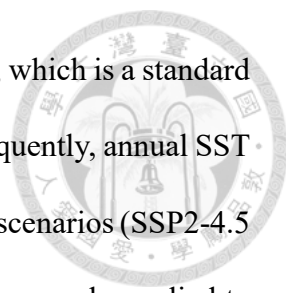
2.2.1 Model Description

Global TIMCOM is an OGCM that includes a sea ice component (CICE4; Hunke et al. (2017)) with 1° nominal horizontal resolution and 55 z-coordinate levels. The horizontal grid is fixed at 1.125° zonally, and varies from approximately 0.3° near the equator to about 0.9° near high latitudes. The vertical grid is linear-exponentially stretched from 10 m at the surface to 500 m at the seafloor. The TIMCOM model adopts a fourth-order-accurate spatial numerical method combining Arakawa A- and C-grids. The time advance is integrated using a modified Robert–Asselin–Williams filtered leapfrog scheme with a time step of 8 minutes in ocean component and 1 hour in sea ice (Williams, 2009; Young et al., 2014), satisfying Courant–Friedrichs–Lewy condition. The vertical mixing is based on the K-Profile Parameterization (Large et al., 1994) with a critical Richardson number of 0.3, and the Gent–McWilliams parameterization is utilized to represent the isopycnal mixing of mesoscale eddies (Gent and Mcwilliams, 1990). The background horizontal diffusivity coefficient is set from 3000 m^2s^{-1} in the surface diabatic layer to 0 m^2s^{-1} at the seafloor. More model details are in Tseng et al. (2022). The topography is slightly smoothed to avoid excess oscillation due to the low resolution with non-dissipative advection scheme, particularly the Ryukyu Island chain and the Japanese coast of Kyushu and Shikoku.

2.2.2 Experiments and Configuration

The sensitivity experiments are motivated by Chen et al. (2019). Firstly, the model is forced by climatological Coordinated Ocean-ice Reference Experiments-Phase II forcing

(Large and Yeager, 2009) for 30 years to spin up the ocean circulation, which is a standard

forcing used in Ocean Model Intercomparison Project (OMIP). Subsequently, annual SST

and wind fields from the mean of the first 30 years in the two warming scenarios (SSP2-4.5

and SSP5-8.5) of the TaiESM1 output (Wang et al., 2021) are simultaneously applied to

the model, while other forcing remains the same with the previous spin-up run. These two

runs (ssp245.ctl and ssp585.ctl, respectively) are designed as the control runs to mimic

the specific forcings in each scenario (Figure 2.1). Finally, from year 60 to year 150,

three sensitivity experiments are proposed: (1) continue the previous run (control run);

(2) apply only the last 30 years' SST from the TaiESM1 warming scenario with others

remaining the same as the control run (SST run), and (3) apply the last 30 years' wind

from the TaiESM1 warming scenario with the others remaining the same as the control

run (wind run). This experimental design (Figure 2.1) aims to investigate the individual

impacts of SST and wind field forcings on the Kuroshio. Here, we want to note that the

long-time natural variability in the Kuroshio system is significant, primarily attributed

to atmosphere (Seager et al., 2001; Qiu and Chen, 2010; Yang et al., 2016). Hence, the

climatological SST or wind forcing is used in this study to reduce the uncertainty arising

from the interannual variability (e.g., Chen et al., 2019).

The SST is strongly nudged towards the SST field in the TaiESM1 warming scenario

through the surface heat flux correction Q, depending mainly on the difference between

prescribed and simulated SST:

$$Q = \frac{dQ}{dt}(SST_{TaiESM1} - SST_{model})$$
$$\frac{dQ}{dt} = C_P \rho \frac{dz}{dt}$$

(2.1)

where $SST_{TaiESM1}$ is the annual SST from the TaiESM1 warming scenario, SST_{model} is the TIMCOM simulated SST, C_P is the seawater heat capacity, and ρ is the seawater density. dQ/dt is a coefficient set to 480 $\text{Wm}^{-2}\text{K}^{-2}$, which is equivalent to a nudging time scale of 5 days for a 50 m mixed layer depth. Note that all other heat fluxes terms are turned off to ensure the imposed nudging heat flux can result in the projected SST consistent with the TaiESM1 warming scenario. All sensitivity experiments are run for another 90 years and the last 50 years are analyzed (Figure 2.1). Figure 2.2 suggests that the quasi-steady equilibrium is reached for the last 50 years. Figure 2.3 also confirms the forcings are correctly imposed.

In the CMIP6 requirement, 10 m zonal and meridional winds are not the standard output. Only 10 m wind speed (U_{10}) is available in the TaiESM1 output. To obtain the 10 m wind directions (u_{10} and v_{10}), the bottom of the 6-hourly pressure coordinate wind velocity (u_p, v_p, often at 60 m height) is utilized. It should be noted that the time interval of wind must be as frequent as possible. If the monthly wind data are used, the wind speed will be overestimated when computing monthly means due to the cancellation of the alternative wind sign change, and leading to an exaggerated u_{10} and v_{10}.

$$
\begin{aligned}
u_{10} &= \frac{U_{10}}{\sqrt{u_p{}^2 + v_p{}^2}} \times u_p \\
v_{10} &= \frac{U_{10}}{\sqrt{u_p{}^2 + v_p{}^2}} \times v_p
\end{aligned}
\tag{2.2}
$$

13
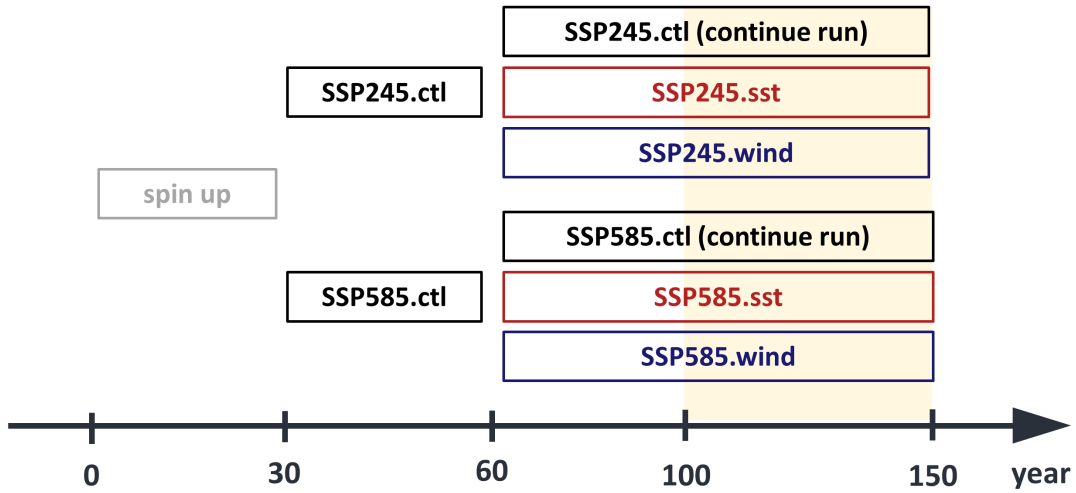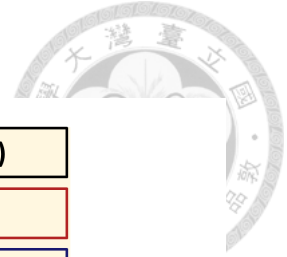
Figure 2.1: Schematic of the global ocean model experiment design.
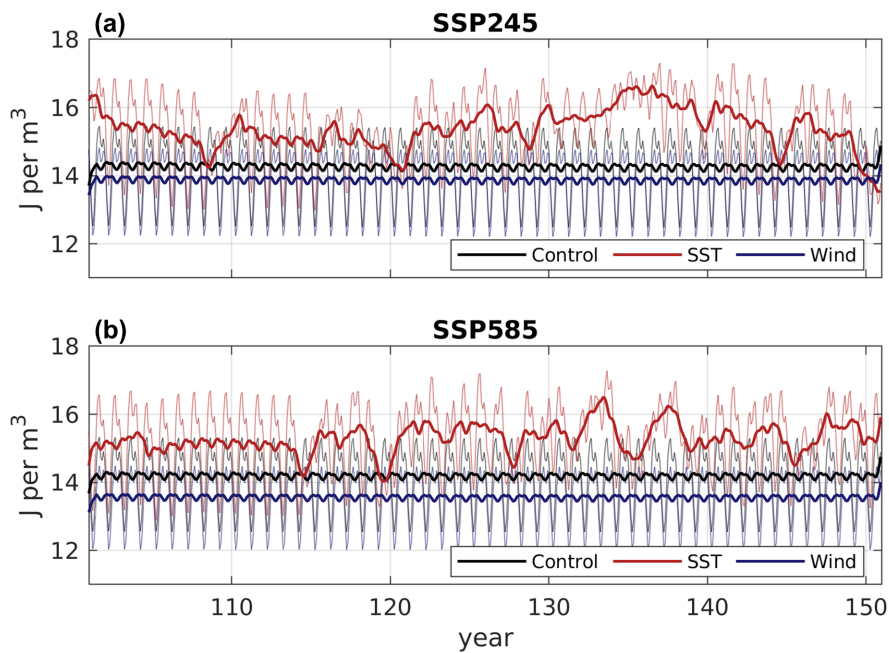
Figure 2.2: Time series of upper 300 m KE in the Kuroshio region (Section 2.3.2) during the last 50 years in (a) SSP2-4.5 and (b) SSP5-8.5 scenario. Thick lines show 13-month running mean.

14
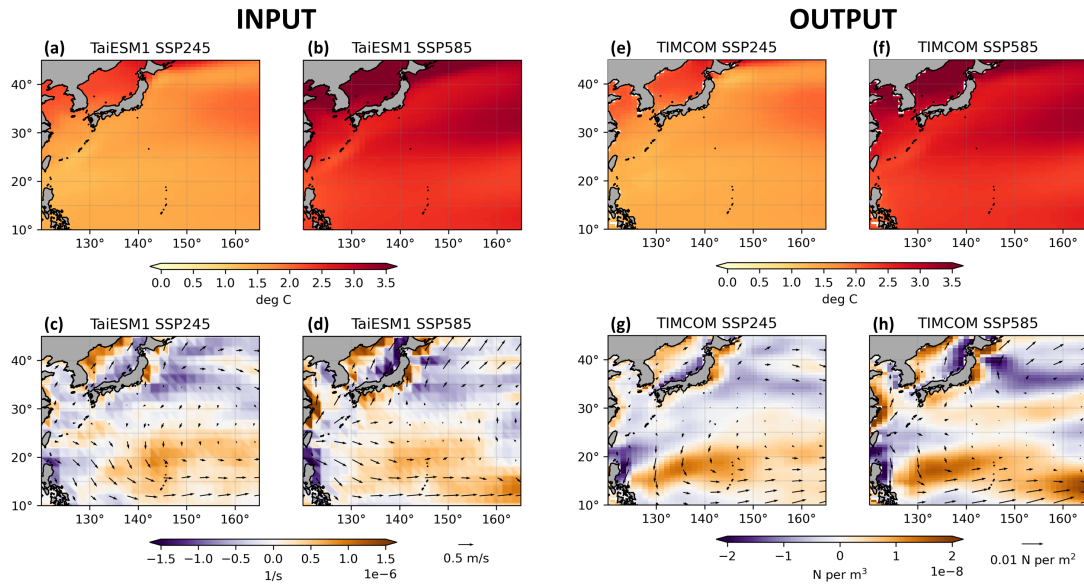
Figure 2.3: (a) The difference of SST between 2071-2099 and 2015-2044 in the TaiESM1 SSP2-4.5 scenario. (b) Same as (a) but for the SSP5-8.5 scenario. (c, d) Same as (a, b) but for the difference of 10 m wind vector and curl (shading). (e) The last 50-year averaged TIMCOM SST difference between SSP245.sst and SSP245.ctl. (f) Same as (e) but for SSP5-8.5 scenarios (SSP585.sst and SSP585.ctl). (g, h) Same as (e, f) but for the wind stress vector and WSC (shading).

2.3 Definitions about Kuroshio

2.3.1 Kuroshio Extension Axis

The KET axis is defined as the position of the maximum kinetic energy (KE) in each longitude between 131 to 150°E. In most LR models, the Tsugaru Strait is only represented by one or a few grids, causing extremely high KE to flow into the interior Pacific Ocean and merge with the KET. Therefore, it is challenging to accurately detect the KET location, as the high KE bias generated by the Tsugaru Strait may be substantial, and its location with the KET may be too close. To minimize the bias from the Tsugaru Strait in each model, we manually select the north boundary when identifying the KE maximum. However, the axes in some models are still located too far north ($\sim 40°$N) (Figure A.1 to A.4), even when compared with the common overshooting position ($\sim 38°$N), and are possibly affected by the bias (e.g., CanESM5, CanESM5-OE, NESM3).

2.3.2 Kuroshio Region

The simulated pathways and spatial distributions of western boundary currents vary among different models. We define the Kuroshio region individually for the CMIP6 ensemble and TIMCOM experiment. The Kuroshio region in CMIP6 is selected by the grid where the upper 300 m meridional transport is greater than 0.25 Sv, encompassing both HR and LR models. In TIMCOM, the region is defined at the upper 300 m meridional transport over 1.125 Sv, which is 4.5 times larger than the CMIP6 because of the zonal grid length (interpolated to 0.25° for CMIP6 models and 1.125° for TIMCOM).

16
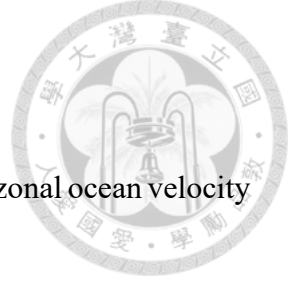
2.4 Barotropic Stream Function

Barotropic stream function (BSF) is calculated by integrating the zonal ocean velocity from the northern boundary:

$$\psi_{Ba} = \int_{-D}^{0} \int_{\phi}^{\phi_N} u r_e \, d\phi dz \tag{2.3}$$

where D is the bottom depth (300 or 1000 m in this study), ϕ is the latitude, ϕ_N is the latitude of the northern boundary (67°N, where the velocity is negligible to the north of the Bering Strait), u is the zonal velocity, r_e is the Earth's radius, and z is the depth.

2.5 Potential Vorticity

Mode water is usually characterized by low potential vorticity (PV) because of its low-stratified (well-mixing, homogeneous) water mass. Additionally, PV is a dynamically conserved variable that can be regarded as a tracer of subtropical ventilation (Hanawa and Talley, 2001):

$$PV = (\zeta + f) \frac{1}{\rho} \frac{\partial \rho}{\partial z} \tag{2.4}$$

where ζ is the relative vorticity, f is the Coriolis parameter (planetary vorticity), ρ is the potential density referenced at the ocean's surface, and z is the depth. The relative vorticity can be neglected here because it is an order less than the planetary vorticity.

17

Chapter 3   Change of Kuroshio in the CMIP6

3.1   Kinetic Energy

Previous studies have indicated that the change tendency of the Kuroshio under global warming varies with depth (Chen et al., 2019; Sen Gupta et al., 2021). To investigate this, we analyze the spatial pattern of KE for the Kuroshio under the SSP5-8.5 warming scenario in different depth (Figures 3.1 and 3.2). We focus on the upper 300 m and 1000 m means of CMIP6 model ensemble, specifically the mean state during the first and last 30 years of the warming projection, spanning from 2015 to 2099. The difference between these two time periods (latter minus former) represents the response to warming.

In the mean state of the LR simulations (Figure 3.1 and 3.2 (d), (e)), the Kuroshio overshoots approximately 3° to an unrealistic high latitude. The KE of the main current is much lower than that in HR simulations (Figure 3.1 and 3.2 (a), (b)), and the KET is too weak to detect. These are common biases that occur when eddies are not properly resolved (e.g., Hurlburt et al., 1996; Choi et al., 2002; Qiu et al., 2015). Furthermore, the position of the ECS-Kuroshio axis is located further east in the LR compared to the HR and the observations. This disparity can be attributed to the smoothing of the Ryukyu Island chain's topography in the LR models, which is necessary for model stability.

Based on the KE change in the HR simulations (Figure 3.1 and 3.2 (c)), it is observed that in both depth, the JP-Kuroshio experiences a dramatic enhancement, while the ECS-

Figure 3.1: (a) The 2015-2044 ensemble mean of upper 300 m KE for HR models. (b) Same as (a) but for 2070-2099. (c) The difference between (b) 2070-2099 and (a) 2015-2044. The blue lines represent the ensemble mean KET axis defined by the maximum current speed. (d, e, f) Same as (a, b, c) but for LR models. Dots indicate areas where over 80% of model members agree on the sign of the trends.

Figure 3.2: Same as Figure 3.1 but for upper 1000 m mean.

20

Kuroshio experiences a slight decrease. The KET axis shifts poleward by approximately

0.6°. On the other hand, in the LR simulations, the entire Kuroshio path shows a marginal

increase in the upper 300 m, and the meridional shift of the KET axis is not obvious ($\sim$

0.2°) (Figure 3.1 (f)). However, in the upper 1000 m, the KE decline in the ECS-Kuroshio

is more evident around the Ryukyu Island chain, while the JP-Kuroshio hardly changes

(Figure 3.2 (f)). In other words, the KE of the ECS-Kuroshio increases in the upper 300 m

and slightly decreases below, indicating a baroclinic change in the LR. The discrepancies

between the LR and the HR suggest that the external forcing from the atmosphere or

the internal ocean dynamic may differ between these two ensembles under the warming

scenario.

3.2   Meridional Transport

Instead of velocity or KE, meridional transport is a more direct variable for quanti-

fying heat transport from low to high latitudes. The first 30 years mean transport of the

ECS-Kuroshio is approximately 20 Sv ($\sim$ 30 Sv) in both the LR and the HR ensembles

within the upper 300 m (1000 m) (Figure 3.3 and 3.4 (a), (d)). However, the zonal gradi-

ent of the BSF here is weaker in the LR than HR, leading to an underestimated KE (i.e.

meridional velocity) shown in the previous section. On the other hand, the mean transport

of the JP-Kuroshio, including the SRG and the KET in the HR, is approximately 35 Sv

($\sim$ 55 Sv) in the upper 300 m (1000 m), which is higher than 25 Sv ($\sim$ 40 Sv) in the LR,

which may be attributed to the mesoscale eddies effect (Qiu and Chen, 2010). Besides, the

Kuroshio overshoots to 40°N in the LR, whereas the KET is confined at 35°N in the HR,

which is more realistic and agrees with the observations. The SRG in the LR is weak and

widely spread south of Japan, while in the HR, it is separated into two main gyres: one to the south and one to the east of Japan, similar to (Cheon et al., 2012). It is interesting to note that the ensemble mean of BSF in the HR exhibits rugged zonal variation, possibly attributed to the local ocean topography (Figure A.5 and A.7).

The changes in BSF under warming are closely related to those in KE. Regardless of the depth in the HR ensembles, the transport of the JP-Kuroshio enhances significantly, particularly in the SRG east of Japan, while the ECS-Kuroshio decreases (Figure 3.3 and 3.4 (c)). On the other hand, the LR ensemble in upper 1000 m also shows a decrease ECS-Kuroshio, with a more moderate enhancement of JP-Kuroshio (Figure 3.4 (f)) compare to the HR. However, in upper 300 m, there is an anticyclonic circulation change surrounding the Ryukyu Island chain (Figure 3.3 (f)), which is not evident in the KE change pattern. By examining the ECS-Kuroshio in more detail with the velocity mean and the change as shown in Figure 3.5, the anticyclonic circulation change indeed exists, and the positive KE change on the west side is greater than the negative change on the east side. The asymmetry in KE change is likely due to the nonlinear term, where the west side of the mean velocity is faster. In other words, the ECS-Kuroshio speeds up in the main axis but also narrows at the same time, resulting in a disagreement changing pattern between KE and transport tendency.

Figure 3.6 presents the vertical profile of meridional transport per unit thickness in the middle of the Ryukyu Island chain to examine the ECS-Kuroshio's baroclinic change. According to the mean state (Figure 3.6 (a), (b)), the simulated transport in the upper layer displays considerable variability among the LR models, with a range of approximately 0.05 Sv/m. The maximum transport value is nearly twice that of the minimum value, high-
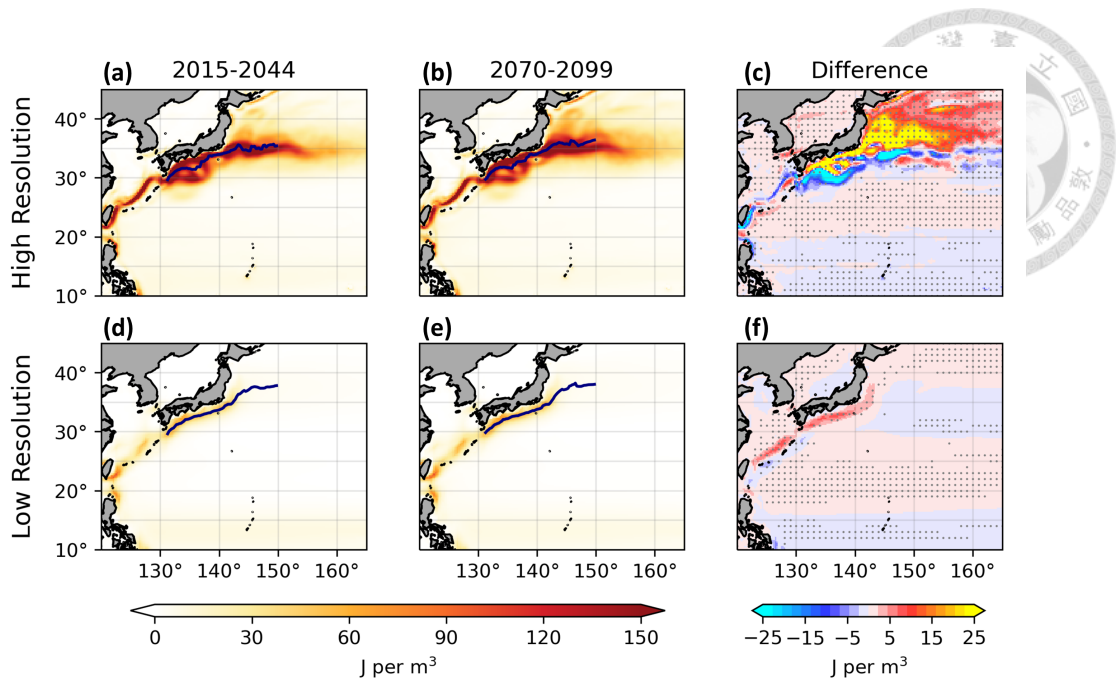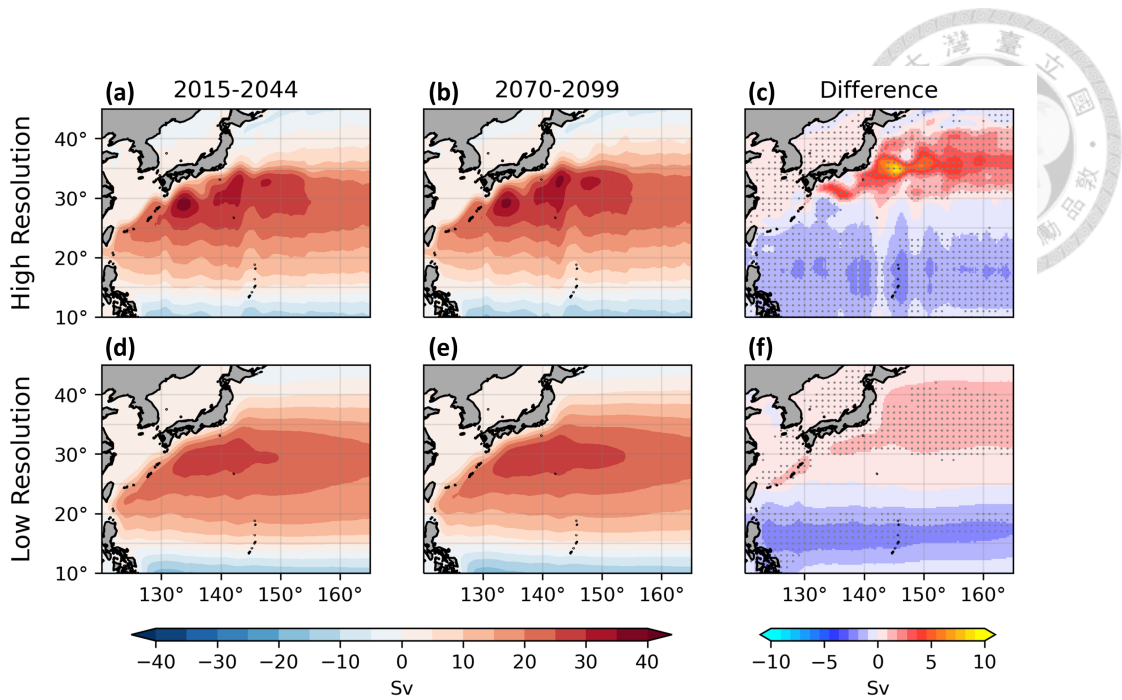
Figure 3.3: (a) The 2015-2044 ensemble mean of upper 300 m BSF for the HR models. (b) Same as (a) but for 2070-2099. (c) The difference between (b) 2070-2099 and (a) 2015-2044. (d, e, f) Same as (a, b, c) but for the LR models. Dots indicate areas where over 80% of model members agree on the sign of the trends.
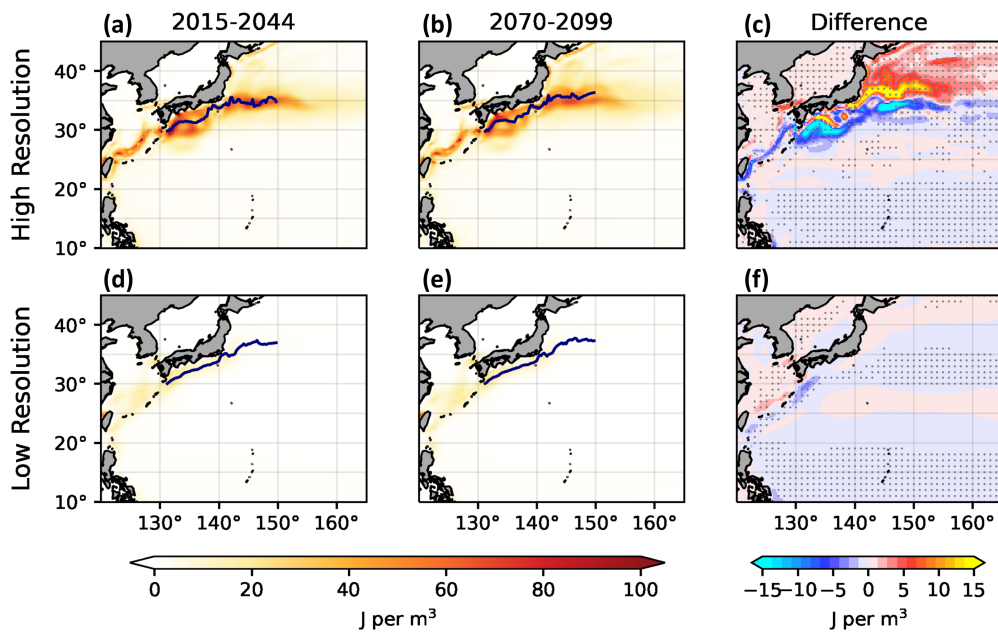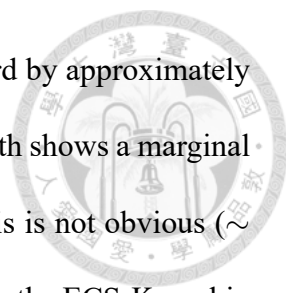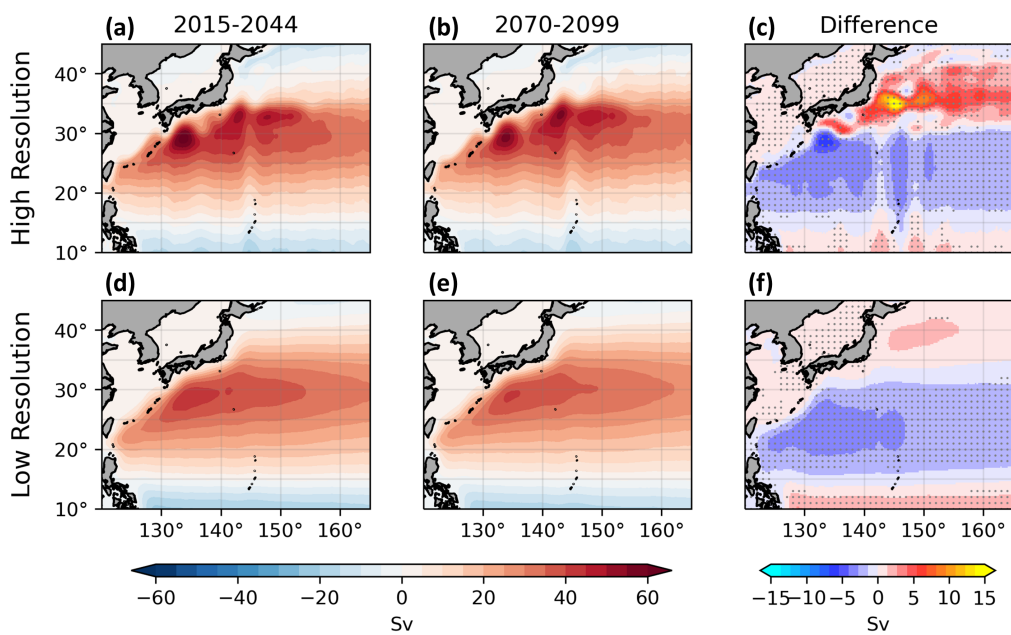

Figure 3.4: Same as Figure 3.3 but for upper 1000 m.

23
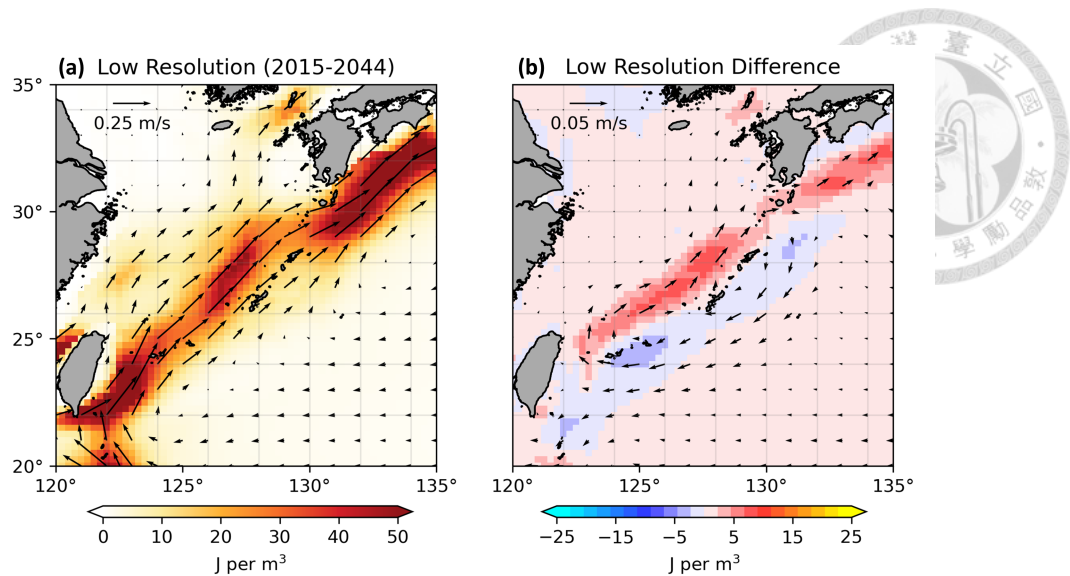
Figure 3.5: (a) The 2015-2044 ensemble mean of upper 300 m current velocity vector and KE (shading). (b) The difference between 2070-2099 and 2015-2044.

lighting the challenges associated with accurately simulating the ECS-Kuroshio within climate models. However, there is no significant difference between the HR and the LR model groups in whole column, which is consistent with the results in Figure 3.3 and 3.4. Note that the AWI-CM-1-1-MR demonstrates an extreme large transport near the surface because our vertical profile includes its SRG, which is located farther south than those of the other models (Figure A.5 and A.7).

Under global warming, the transport remains nearly unchanged in the upper 200 m due to the anti-cyclonic change around the Ryukyu Island chain (Figure 3.6 (c)), as clarified in Figure 3.5 (b). However, the transport change tends to decrease in the deeper layer, consistent with the findings in Figure 3.4 (c), (f). The transport change of each model in the upper layer demonstrates a dispersed distribution. However, among the 5 HR models, 4 of them exhibit changes that fall below the lower quartile. Apart from GFDL-CM4, the HR models do not exhibit the baroclinic change shown in the ensemble and most of the

24

LR, suggesting that the consistent baroclinic change is not as evident in HR.
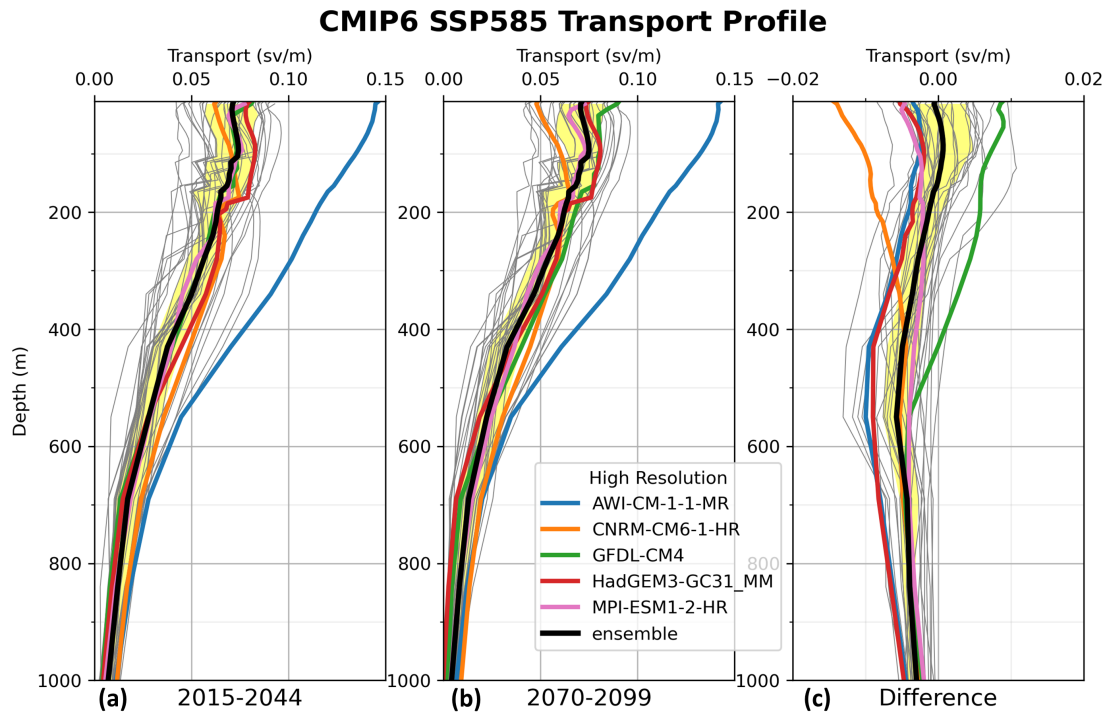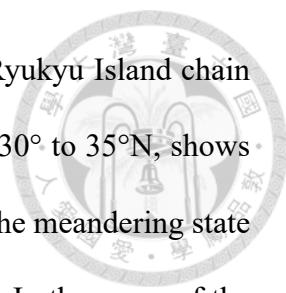
Figure 3.6: (a) The 2015-2044 mean of meridional transport profile at 26.75°N, integrating from 125 to 132°E (around the Ryukyu Island chain). (b) Same as (a) but for 2070-2099. (c) The difference between (b) 2070-2099 and (a) 2015-2044. Colored, gray, and black lines indicate HR models, LR models, and all 33 model ensembles, respectively. Yellow shading indicates the interquartile range.

The zonally integrated meridional transport at various latitudes and depths reveals varying strengths and changes in different parts of the Kuroshio. Regardless of the depth, the largest mean transport of the Kuroshio occurs in the ECS, around 25° to 30°N, where the zonal range of the Kuroshio is also the widest, including the Tsushima Strait as described in Section 2.3.2 (Figure 3.7 and 3.8 (a), (b)). The ECS-Kuroshio transport exhibits consistency among the HR simulations excluding the AWI-CM1-1-MR, whereas it displays greater spread in the LR simulations. This discrepancy, also shown in Figure 3.6,

25

may arise from the difference in inaccurate topography around the Ryukyu Island chain among the LR models. On the other hand, the JP-Kuroshio, around 30° to 35°N, shows more pronounced fluctuations in the HR than the LR, attributable to the meandering state among the HR that can only be captured in eddy-permitting models. In the mean of the first 30 years of the HR, the majority of maximum transport values are located around 30°N, where the SRG enhances the speed of the Kuroshio. The SRG in AWI-CM1-1-MR is located more south, so the maximum transport values is at around 28°N.

The ensemble of transport distribution and location of the peak remain unchanged under warming period (Figure 3.7 and 3.8 (b)). However, both the transport magnitude and fluctuations increase significantly towards the north by 30°N in the HR (Figure 3.7 and 3.8 (c)). Nevertheless, in the LR, the ECS-Kuroshio is nearly unchanged (decrease) in the upper 300 m (1000 m), while in the HR, a decrease is observed across the entire 1000 m column. These results align with the finding presented in Figure 3.6 (c).
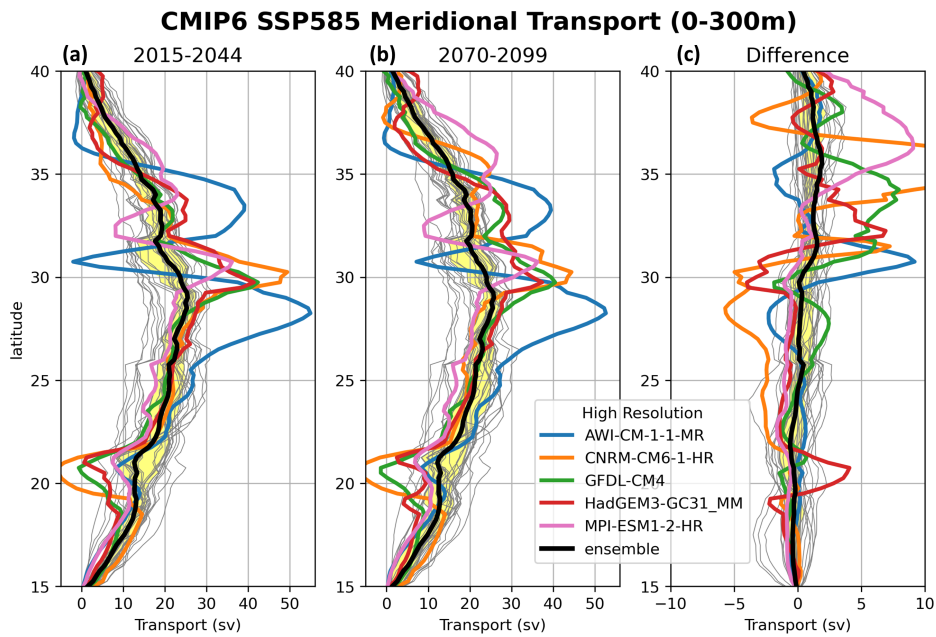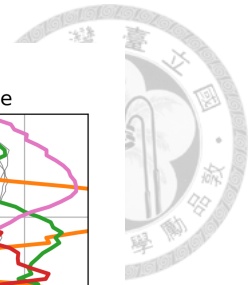
Figure 3.7: (a) The 2015-2044 mean of upper 300 m meridional transport by latitude, which zonally integrates the Kuroshio region defined in Section 2.3.2. (b) Same as (a) but for 2070-2099. (c) The difference between (b) 2070-2099 and (a) 2015-2044. Colored, gray, and black lines indicate HR models, LR models, and all 33 model ensembles, respectively. Yellow shading indicates the interquartile range.
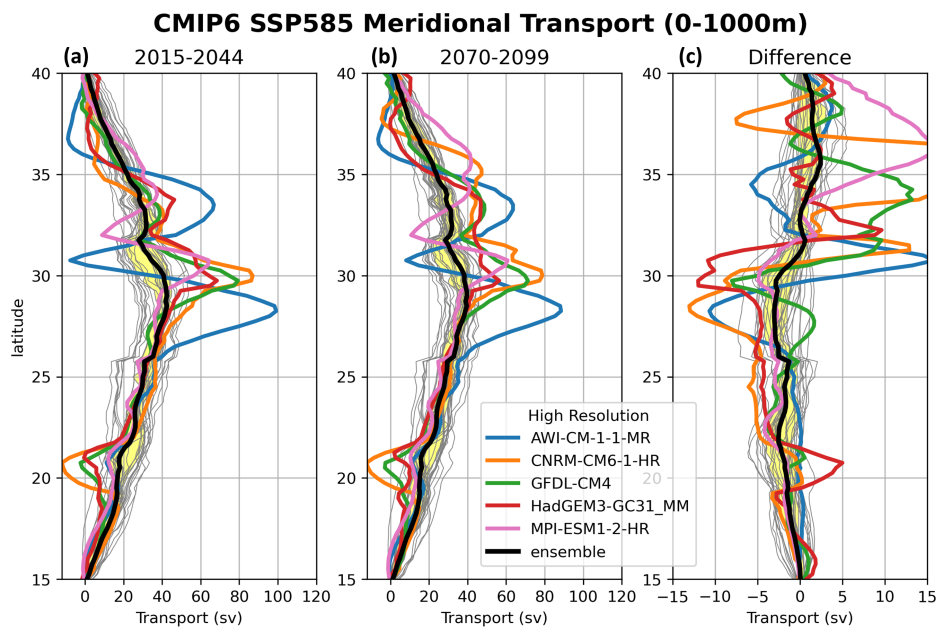
Figure 3.8: Same as Figure 3.7 but for upper 1000 m.

3.3   Wind Stress Curl Relation

According to the Sverdrup theory, the subtropical gyre is driven by negative WSC (i.e., subtropical high), and therefore, the WSC change can directly affect the gyre speed, including the western boundary current. The negative WSC becomes weaker towards the south by 30°N, while it becomes stronger towards the north, thus forming a dipole-like changing pattern (Figure 3.9). This also implies that the mid-latitude zero WSC line (i.e., midlatitude westerly wind) shifts poleward due to the Hadley cell expansion (e.g., Lu et al., 2007; Davis and Birner, 2022). The WSC changes in both of the two regions are more pronounced in the HR than in the LR ensemble, which may be attributed to wind or current change based on the wind stress algorithm. The dipole distribution of the WSC change is consistent with the spatial pattern of KE and meridional transport, which can also be separated into the ECS-Kuroshio and the JP-Kuroshio, except LR in upper 300 m. Hence, scatter plots and linear regression analysis of the WSC and meridional transport change of the Kuroshio are presented to further investigate the relation.

Due to the substantial differences in the mean of the Kuroshio's KE and the meridional transport among different models (with the HR simulations exhibiting much higher intensity than the LR simulations), the analysis focuses on relative changes. The negative relations between the WSC and the transport change are significant in the ECS-Kuroshio, regardless of the depths (p-value < 0.05, Figure 3.10 (b), (d)). However, the negative relation with KE is insignificant in the upper layer, in which the p-value is 0.1 (Figure 3.10 (a)). Distribution of different colored markers indicate that the ocean components used in each couple model lie along the same regression line. This demonstrates that the
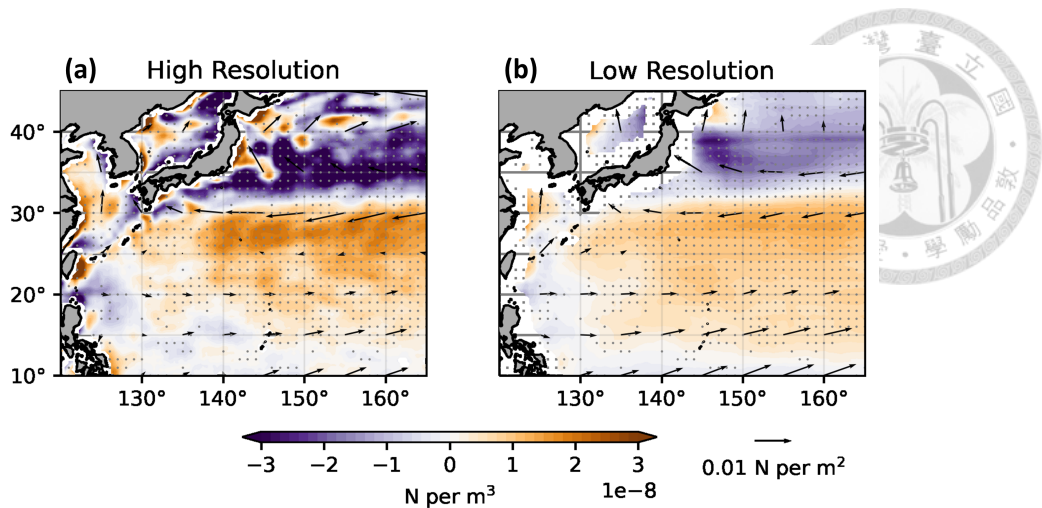
Figure 3.9: The ensemble difference of wind stress vector and WSC (shading) between 2070-2099 and 2015-2044 for (a) HR and (b) LR models. Dots indicate areas where over 80% of model members agree on the sign of the trends.

relation between the WSC and transport is independent of the specific ocean models used. Moreover, those HR markers labeled with red circles, except CNRM-CM6-1-HR, also share the same regression line with LR, suggesting that the difference of ECS-Kuroshio change among CMIP6 models including HR could also be attributed to the magnitude of wind force changes in the atmosphere.

In the JP-Kuroshio, the negative relations between the WSC and the transport change are also significant (Figure 3.11 (b), (d)), while the relations with KE are positive and insignificant (Figure 3.11 (a), (c)) in both depth range. This is because the Kuroshio begins to separate and turn towards the east, and the dynamic here is more complicated—it needs to consider not only wind, but also topography, etc. It is worth noting that the transport of the HR is more sensitive to the WSC changes than that of LR in both depths (with the HR having a steeper regression line), suggesting that the dynamics that can only be resolved in the HR may take place during global warming.
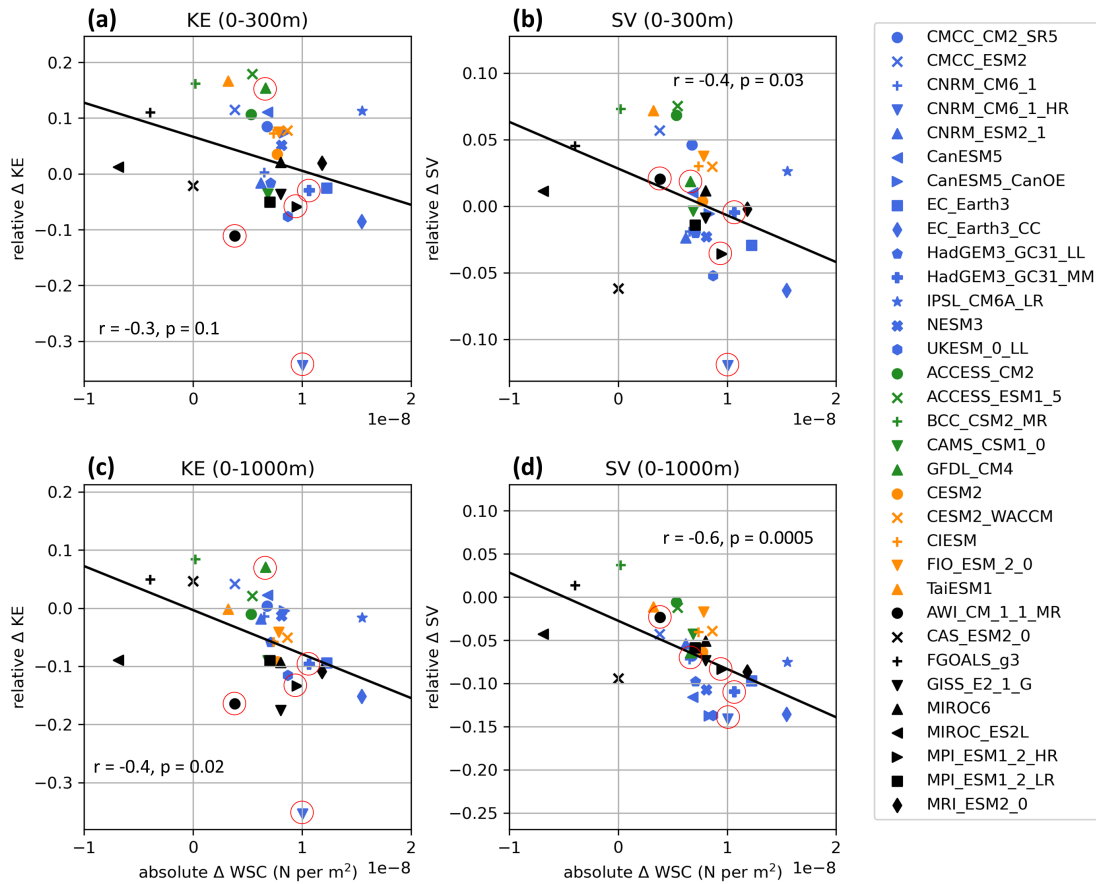
Figure 3.10: (a) Scatter plots of absolute WSC change against relative KE changes in the upper 300 m ECS-Kuroshio. The WSC change is defined as the mean of the region (120°-165°E, 20°-30°N). (b) Same as (a) but for relative meridional transport changes. (c, d) Same as (a, b) but for upper 1000 m ECS-Kuroshio. The blue, green, orange, and black markers indicate the ocean model based on NEMO, MOM, POP, and others, respectively. Red circles indicate HR.
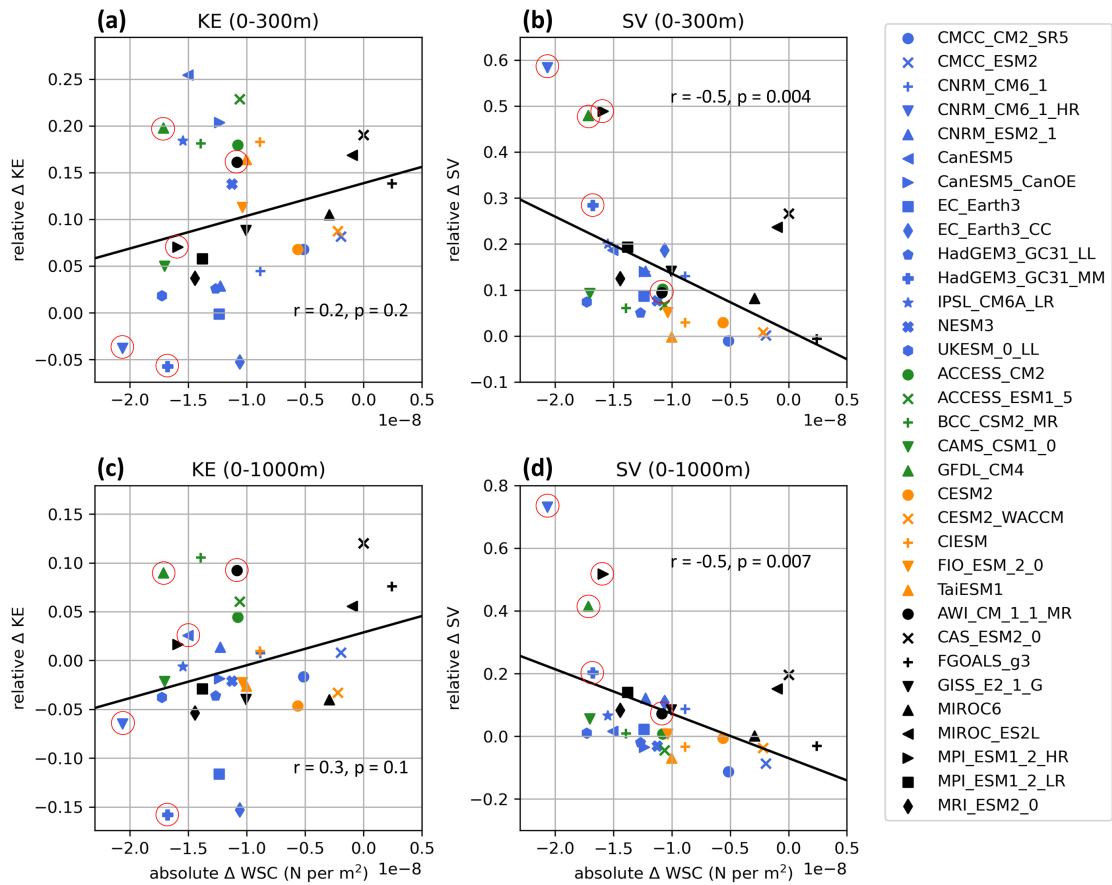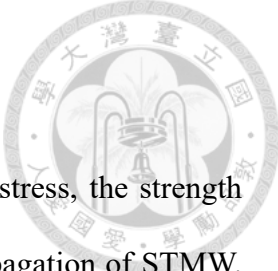
Figure 3.11: Same as Figure 3.10, but for the JP-Kuroshio, defined as the mean of the region (140°-165°E, 32°-42°N).

3.4 Vertical Thermal Structure

Chen et al. (2019) declared that instead of the impact of wind stress, the strength of the Kuroshio in the upper layer is dominantly affected by the propagation of STMW. In this study, STMW is identified using the criteria of low PV (Section 2.5) to compare the differences between the LR and HR models under global warming. Two vertical sections, P13 (165°E) and P09 (137°E), are analyzed to determine the STMW's position and characteristics (Figures 3.12 and 3.13).

In the P13 sections, STMW is primarily distributed at approximately 100 m to 400 m in the first 30 years of the warming simulation, where the vertical gradient of density is small, indicating efficient mixing of water masses (Figures 3.12 (a), (d)). In the HR, the depth of the STMW bottom is deeper compared to the LR. However, the PV values are higher in the HR, suggesting that while the mixing depth extends to a greater depth in the HR, the mixing itself is less uniform compared to the LR. Besides, because the STMW subducts south of the KET (Hanawa and Talley, 2001; Douglass et al., 2013), the STMW's north boundary is located at 35°N in the HR, while it overshoots to 40°N in the LR. In the P09 section, the mean STMW is observed at latitudes ranging from 25° to 30°N and depths between 200 m and 400 m (Figures 3.13 (a), (d)) in both resolutions. The presence of a low PV signal is less pronounced compared to the P13 section because it is located towards the end of the STMW pathway.

During global warming, the bottom layer of the STMW becomes shallower, and the PV increases due to enhanced stratification by surface heating, which prevents seawater from mixing into a deeper layer in both sections (Figure 3.12 and 3.13 (b), (e)). Similar

32

results are also shown in Wang et al. (2013). Note that even in the first 30 years of the warming simulation, the bottom layer of the STMW is shallower than usual, which can normally reach up to around 500 m (Wang et al., 2013; Douglass et al., 2013; Tsubouchi et al., 2016; Wu et al., 2021). This means that the thickness of the STMW is sensitive to the stratification.

The density changes under warming are primarily influenced by temperature changes (Figure 3.12 and 3.13 (c), (f); salinity change is shown in Figure A.14 and A.15 (c), (f)), which is also supported by Zhang et al. (2017). Although the STMW transport decrease under warming scenarios, the LR models still exhibit a subsurface warm water pattern which distribute along the isopycnal from mid-latitude to 20°N in both P13 and P09 sections. In contrast, the HR models' subsurface warm water is restricted to around 30°N. The warm water pattern along the sections is more likely to correspond to the STMW pattern in LR. The different pathways and volume of warm water between HR and LR may lead to a different dominant mechanism for the Kuroshio change under global warming.

Figure 3.14 shows the vertical section (26.75°N) through the middle of the ECS-Kuroshio to clarify the warm water transport. The Kuroshio can be identified at 126°E in the profile by the location of the high mean potential temperature and the seawater (Figure 3.14 (a), (b), (d), (e)). There is a slightly less pronounced warming change in the both LR and HR simulations in 126° to 130°E and 129°E, respectively (Figure 3.14 (c), (f)), probably attribute to the topography of Ryukyu Island chain. The same feature is also shown in Chen et al. (2019) (their Figure 9 and 10). In the LR, the warming water located to the east of the Kuroshio is more obvious, as supported by the P09 and P13 vertical sections, where the warm water corresponding to the STMW are also more pronounced in
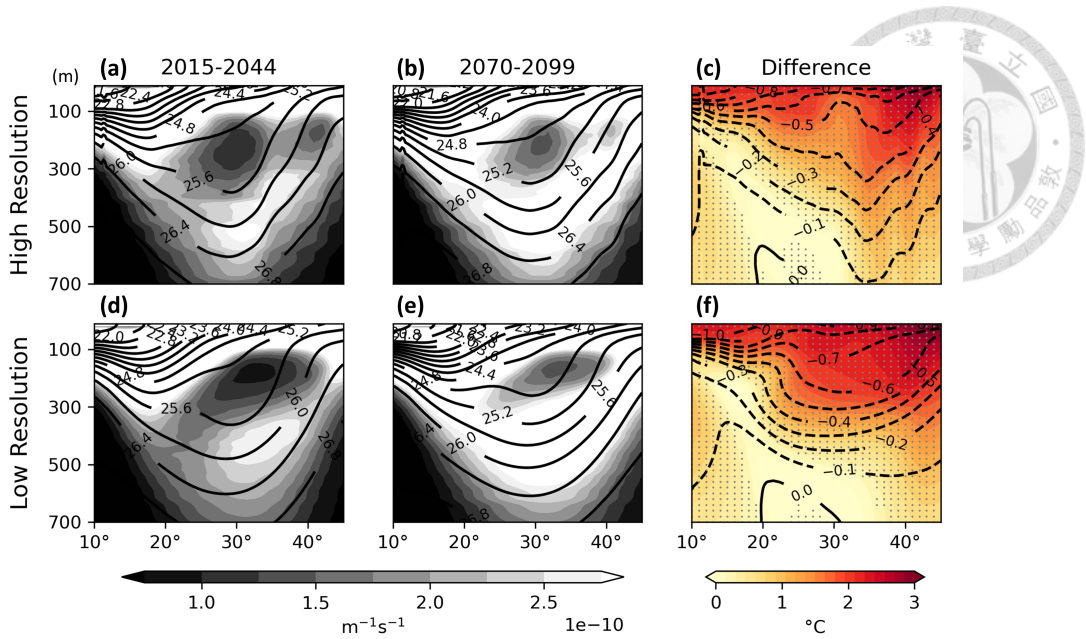
Figure 3.12: Vertical cross section along the P13 (165°E). (a) The 2015-2044 ensemble mean of potential density (contour) and potential vorticity (shading) for HR models. (b) Same as (a) but for 2070-2099. (c) The difference of potential density (contour) and potential temperature (shading) between (b) 2070-2099 and (a) 2015-2044. (d, e, f) Same as (a, b, c) but for LR models. Dots indicate areas where over 80% of model members agree on the sign of the trends.
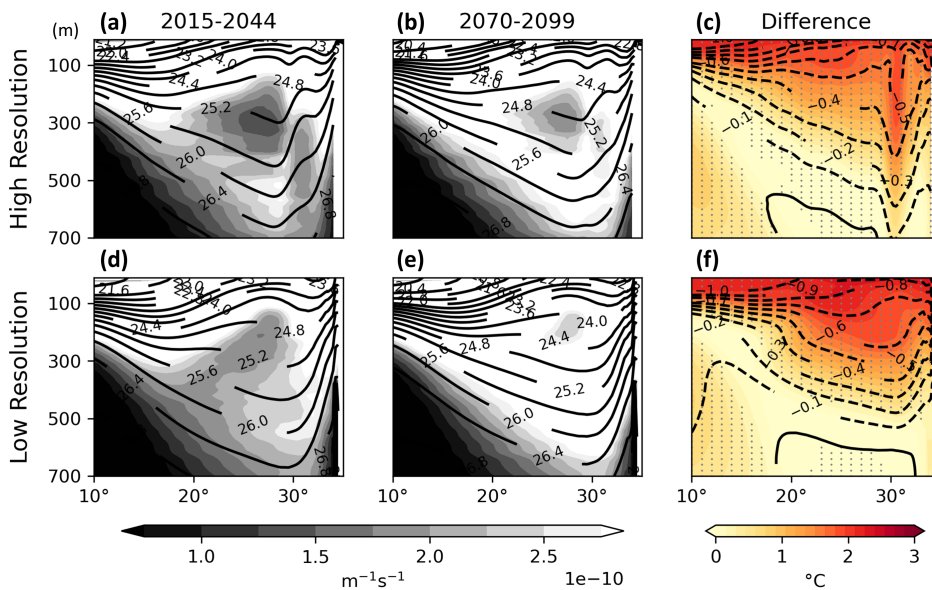
Figure 3.13: Same as Figure 3.12 but for the vertical cross section along P09 (137°E).

the LR. Although these uneven warming patterns provide evidence of enhanced thermal wind relation, the underlying reasons for the difference between LR and HR need further examination.
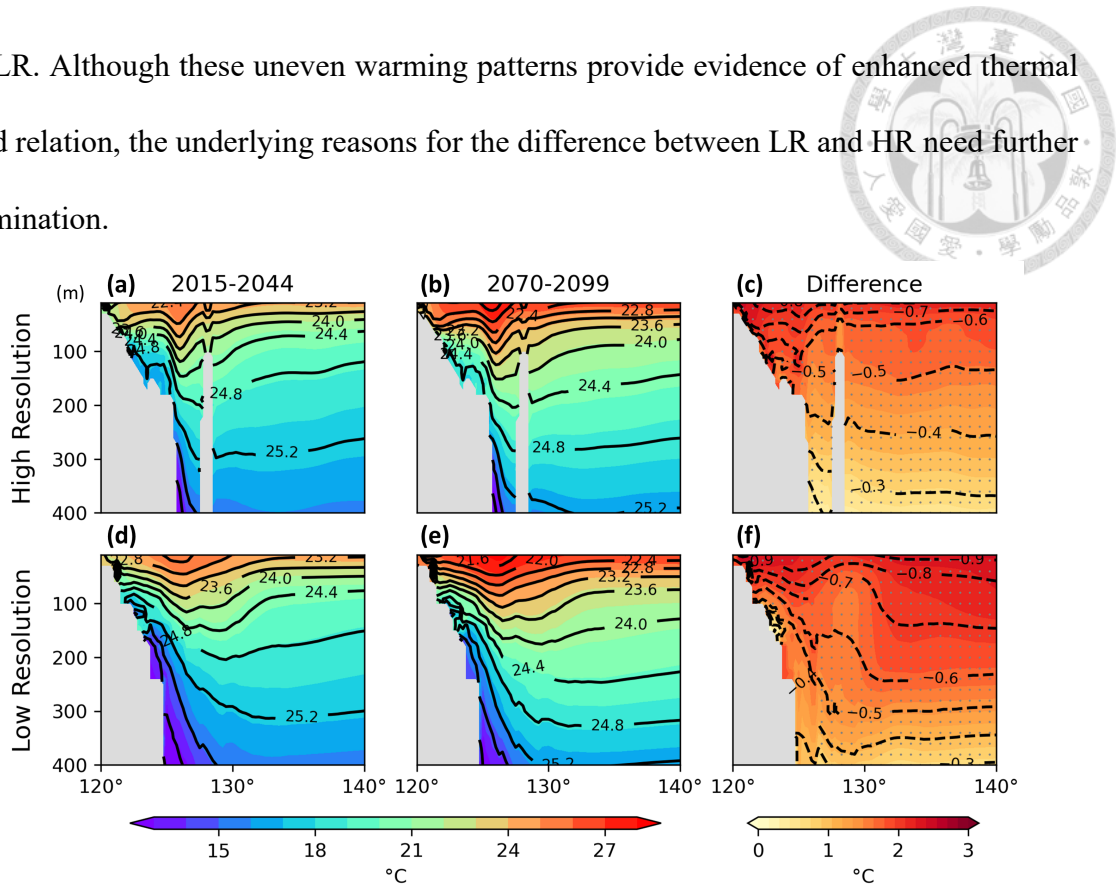
Figure 3.14: Vertical cross section along the zonal profile of the ECS-Kuroshio (26.75°N). (a) The 2015-2044 ensemble mean of potential density (contour) and potential temperature (shading) for HR models. (b) Same as (a) but for 2070-2099. (c) The difference between (b) 2070-2099 and (a) 2015-2044. (d, e, f) Same as (a, b, c) but for LR models. Dots indicate areas where over 80% of model members agree on the sign of the trends.

35
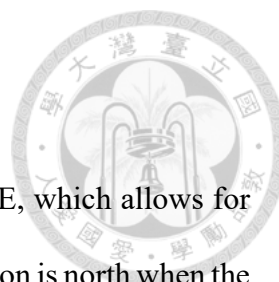
3.5 Large Meander

Figure 3.15 shows the location of the Kuroshio axis along 135°E, which allows for identification of the Kuroshio path type (Ambe et al., 2004). The position is north when the Kuroshio axis flows along the south Japanese coast, whereas it is south when a large meander state occurs. During the LR simulations, due to the overshoot and lack of mesoscale eddies activity (Tseng et al., 2012), the Kuroshio remains at a non-large-meander path. However, among the HR simulations, the frequency of large meander state transitions in AWI-CM-1-1-MR, CNRM-CM6-1-HR, and HadGEM3-GC31-MM decreases during the warming scenario. In contrast, MPI-ESM1-2-HR shows no meander signal as it has the coarsest resolution among the HR models. Additionally, AWI-CM-1-1-MR, CNRM-CM6-1-HR, and GFDL-CM4 indicate a northward migration of the Kuroshio axis under the simulation.
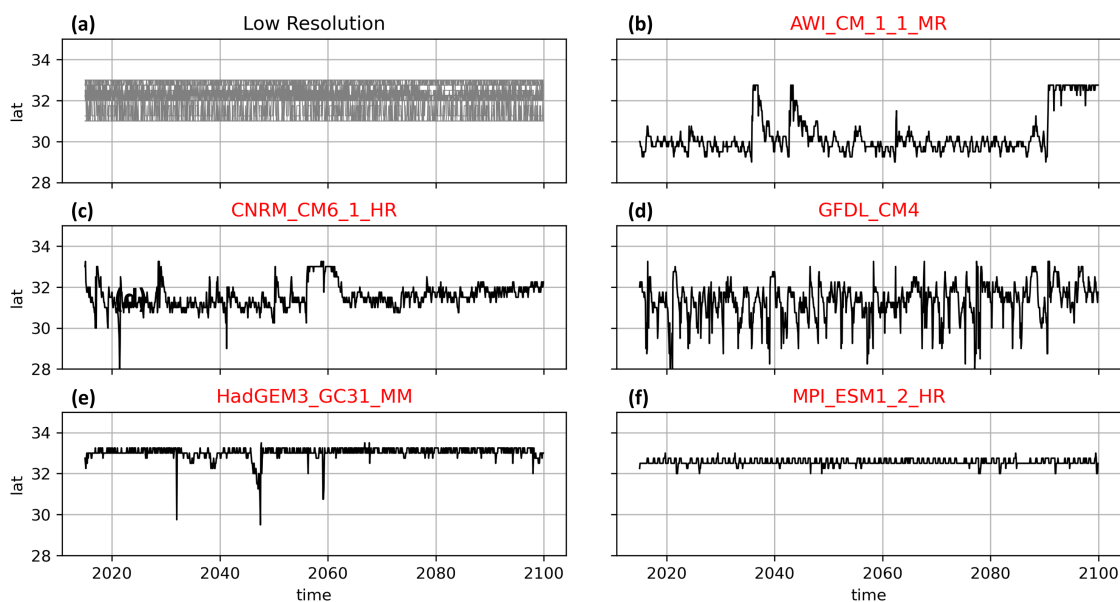
Figure 3.15: Location of the Kuroshio axis along 135°E during the SSP5-8.5.

36
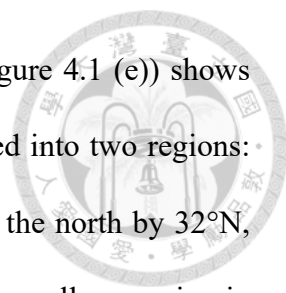
Chapter 4   TIMCOM sensitivity experiments

4.1   Dynamical Changes

In order to identify the primary driver of the Kuroshio change during global warm-
ing, we consider the impact of wind change and SST change (i.e., by surface heating),
respectively, for different warming scenarios (Figure 2.3). As is commonly simulated in
the LR models, the Kuroshio system overall, regardless of different runs (Figure 4.1 and
4.2 (a), (b), (d)), show a weaker mean KE while the Kuroshio path is closer to the Ryukyu
Island chain compared to the observations due to the broader band of modeled Kuroshio
Tseng et al. (2016). As the simulated Kuroshio separation weakly overshoots along the
east coast of Japan, the simulated KET path (blue line) indicates a nearly non-overshoot
pathway. In addition, the Kuroshio path east of Luzon and Taiwan is also more offshore
and jagged compared to other LR models in CMIP6 (Figure A.1 and A.3), possibly due
to the lack of topographical smoothing and the fourth-order-accurate spatial discretization
scheme.

Under the SSP2-4.5 scenario, the KE in the Kuroshio is enhanced along the entire
path due to the SST change, while the KET axis does not shift meridionally (Figure 4.1
(c)). A more intense SST warming can be found between 145° to 165°E rather than along
the east coast of Japan (Figure 2.3 (a), (e)). As a result, the KET region tends to shift
equatorward due to the thermal wind balance.

On the contrary, the wind run under the SSP2-4.5 scenario (Figure 4.1 (e)) shows that the upper 300 m KE response of the wind change can be divided into two regions: a decrease to the south of Japan by around 32°N and an increase to the north by 32°N, respectively. This dipole-like change possibly results from the Hadley cell expansion in the projected future scenario (e.g., Lu et al., 2007; Davis and Birner, 2022). The zero WSC line shifts poleward so that the WSC change becomes the dipole-like pattern. This feature can be seen in all CMIP6 models (but magnitude varies with models), including TaiESM1 (Figure 3.9, 2.3 (c), (g) and A.9). The magnitude of the KE change in the southern part is greater than that in the northern part. The differences of KE pattern suggest that the Kuroshio along the coast of south Japan shifts northward, but the Kuroshio axis including the KET shows an insignificant shift. In short, our individual sensitivity study under the SSP2-4.5 scenario shows the response to the surface warming is larger than that to the wind stress change, suggesting the dominant role of surface warming for the whole path of Kuroshio. These results are similar to Chen et al. (2019) and Peng et al. (2022).

Figures 4.2 (c) and (e) show a similar change under the SSP5-8.5 scenario to the SSP2-4.5 scenario. These patterns suggest a more reduced magnitude along the south coast of Japan in the wind run under the SSP5-8.5 scenario while the enhanced magnitude of change in the SST run has no significant difference between these two scenarios. This result indicates that the KE in the Kuroshio is more sensitive to the atmospheric wind stress change. However, the response of the SST change in the south coast of Japan and ECS is still slightly greater than the wind stress change under the SSP5-8.5 scenario, confirming the dominant surface warming in both scenarios. The response of the BSF shows corresponding patterns with KE change (Figure A.17 and A.18).
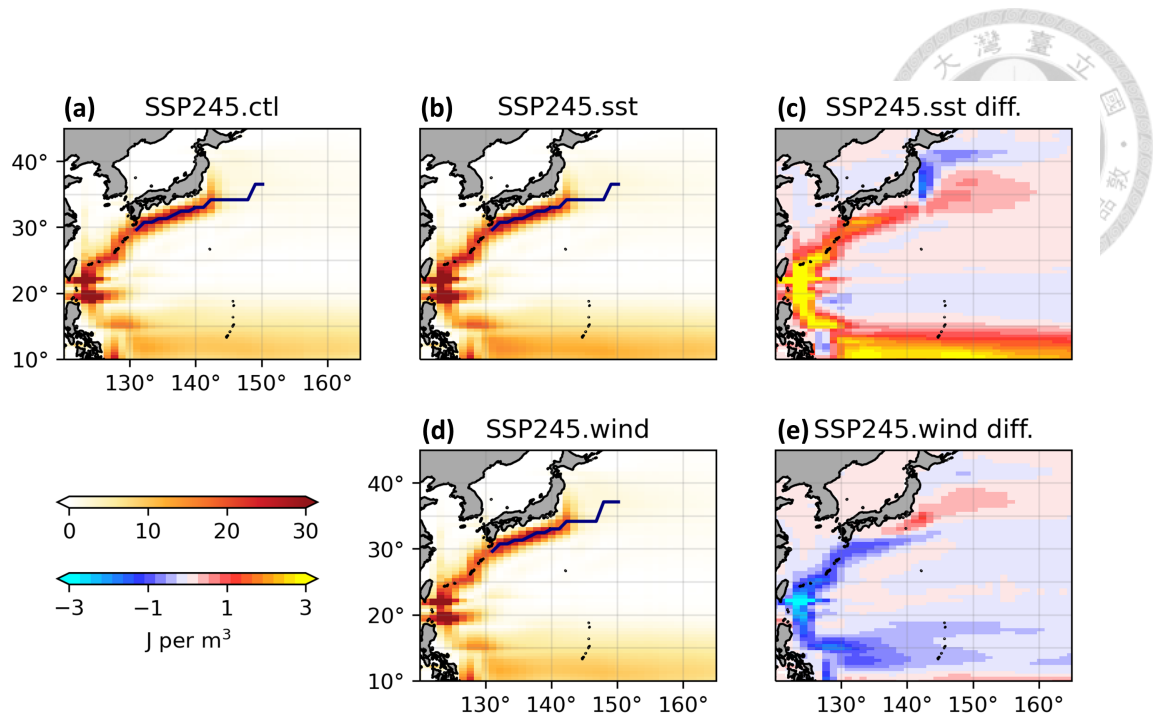
Figure 4.1: The upper 300 m mean KE in (a) SSP245.ctl and (b) SSP245.sst. (c) The difference between (b) SSP245.sst and (a) SSP245.ctl. (d, e) Same as (b, c) but for SSP245.wind. The blue line represents the mean KET axis in each run.
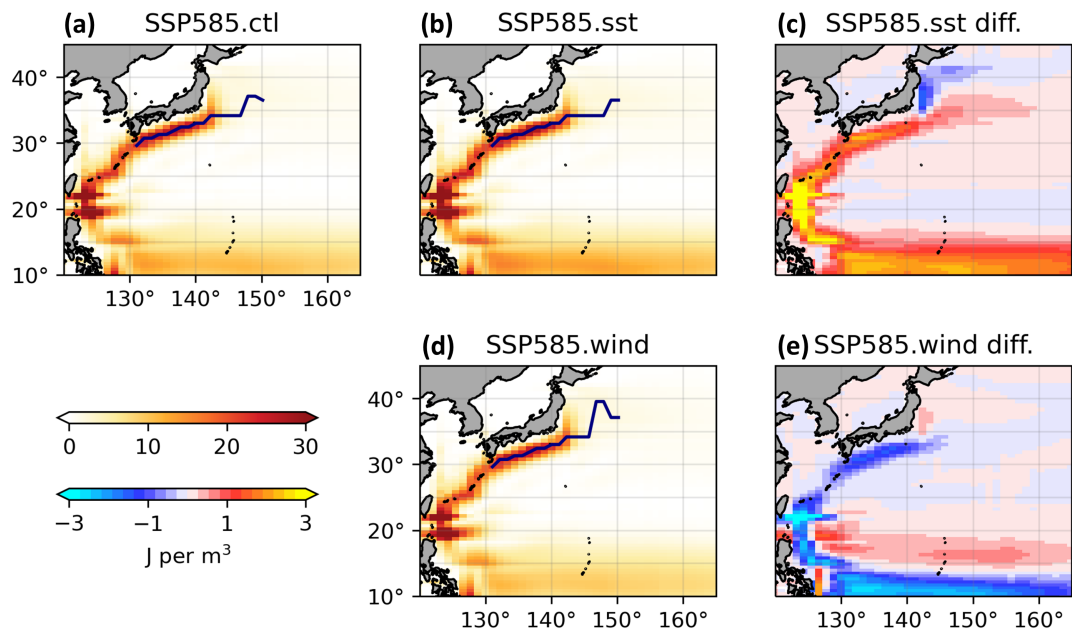
Figure 4.2: Same as Figure 4.1 but for the SSP5-8.5 scenario.
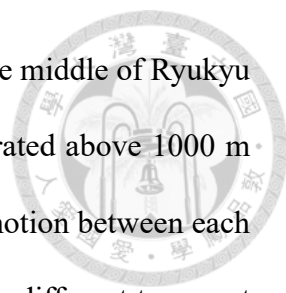
Figure 4.3 (a) shows the mean meridional transport profiles at the middle of Ryukyu Island chain across 26.75°N section. The ECS-Kuroshio is concentrated above 1000 m and almost vanishes below the depth. The difference of layer of no motion between each scenario is less than 100 m. Moreover, the enlarged figure shows the different transport of each run in the upper 300 m, indicating that the current shear of each run in upper layer is modified by our forcings, which also supposed by (Chen et al., 2019) and Peng et al. (2022). Figure 4.3 (b) shows the transport difference between each sensitivity test and control run. The transport response to wind changes a lot in different scenarios, while a similar response shows in those SST runs. This indicates that the ECS-Kuroshio change is more sensitive to the wind change. In the upper 300 m, the response to surface warming is found to be greater than that to the wind stress change, with the largest change at around 200 m in both scenarios. However, below 300 m, the impact of surface warming decreases rapidly, and the influence of wind becomes more pronounced than the SST, especially in the SSP5-8.5 scenario. The results suggest that the surface warming dominates the ECS-Kuroshio change in the upper 300 m in both scenarios, while the wind dominates below 300 m, notably in the SSP5-8.5 scenario.

4.2   Thermal Structure Changes

Similar to Section 3.4, we further examined the vertical sections along P13 (165°E) and P09 (137°E) to investigate the transport and change of the warming water and STMW in the SST warming sensitivity experiment. In P13, the control run of both scenarios (Figure 4.4 (a) and (d)), where the SST is abruptly nudged to the mean of the first 30 years in the warming scenario, the stratification is strong, resulting in a bottom layer of STMW
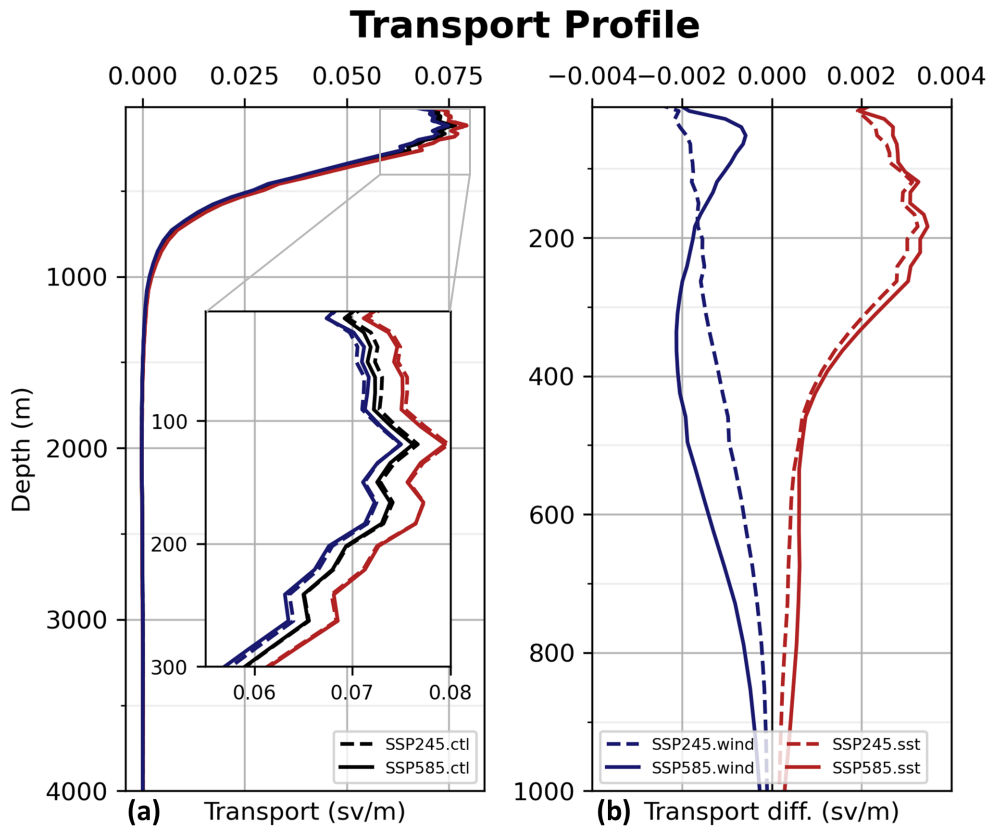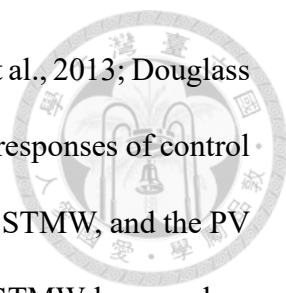
Figure 4.3: (a) The mean meridional transport profiles across 26.75°N, integrating from 125 to 132°E. The black, red and blue solid lines indicate SSP585.ctl, SSP585.sst and SSP585.wind runs, respectively. Dashed lines are for SSP2-4.5 scenario. (b) The difference between the SST / wind runs and control runs in SSP5-8.5 (solid lines) and SSP2-4.5 (dashed line) scenario.

less than 300 m, which is already shallower than observations (Wang et al., 2013; Douglass et al., 2013; Tsubouchi et al., 2016; Wu et al., 2021). Compare to the responses of control run, the SST run in both scenarios (Figure 4.4 (b), (e)) show a thinner STMW, and the PV of the STMW increase. This suggests that the characteristics of the STMW become less pronounced, which is similar to the findings in CMIP6. Besides, under the more severe warming scenario (Figure 4.4 (d), (e)), the PV of the STMW exhibits a more notable increase in the SST run. This simulation outcome can be attributed to the intensified surface heat flux, which enhances the stratification in the ocean and hinders the generation of STMW by suppressing vertical mixing.

Despite the reduced thickness of the STMW in our runs, the SST run still exhibit warm water patterns along 23.6 to 25.6 kg/m^3 isopycnal, which is the primary distribution region of the STMW (Figure 4.4 (c), (f)). However, these warm water distribution in both scenarios differ from those CMIP6 low resolution ensemble in the tropical region (south of 20°N, Figure 3.12 (f)), suggesting that factors other than SST warming contribute the warm water distribution here.

In P09 section, the mean PV is almost identical between each run (Figure 4.5 (a), (b), (d), (e)). The warm water also exist along 23.6 to 25.6 kg/m^3 isopycnal, south of 25°N (Figure 4.5 (c), (f)). The warmest water in the section is found at a subsurface depth of approximately 200 m, rather than at the surface where the heat flux is directly enforced. This implies that the source of heating here is not from vertical mixing but rather from horizontal advection. These are all clues that the transport of warm water occurs along isopycnal.
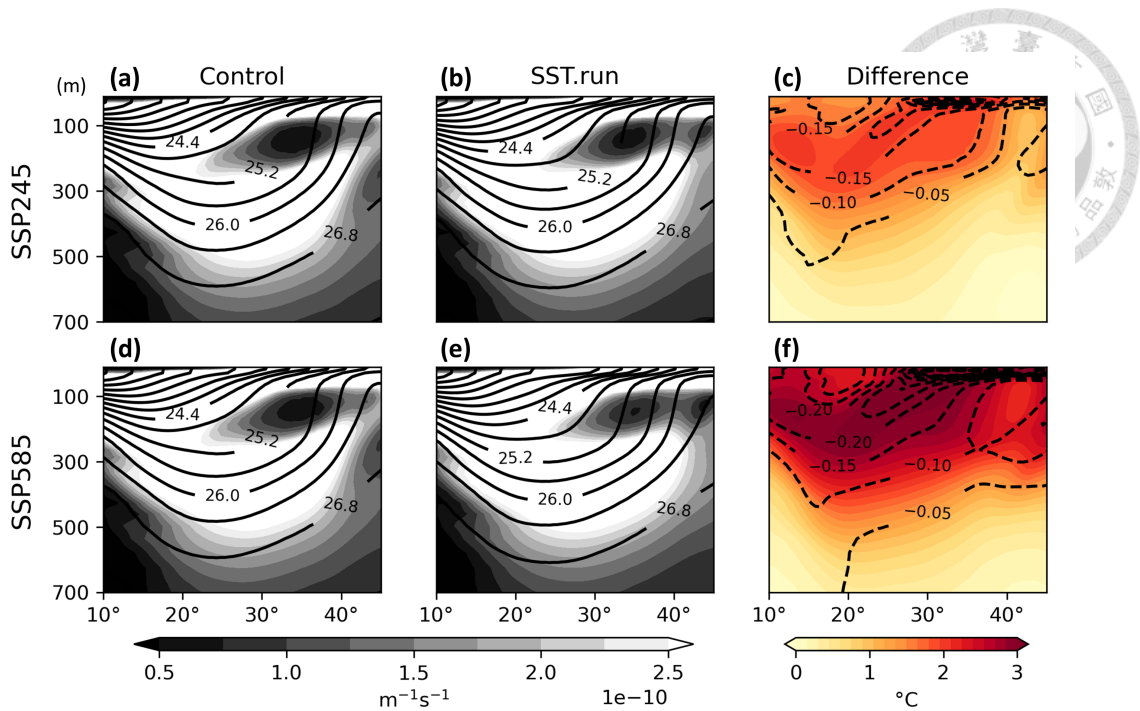
Figure 4.4: Vertical cross section along the P13 (165°E). The mean potential density (contour) and potential vorticity (shading) in (a) SSP245.ctl and (b) SSP245.sst. (c) The difference between (b) SSP245.sst and (a) SSP245.ctl. (d, e, f) Same as (a, b, c) but for SSP5-8.5 scenario.
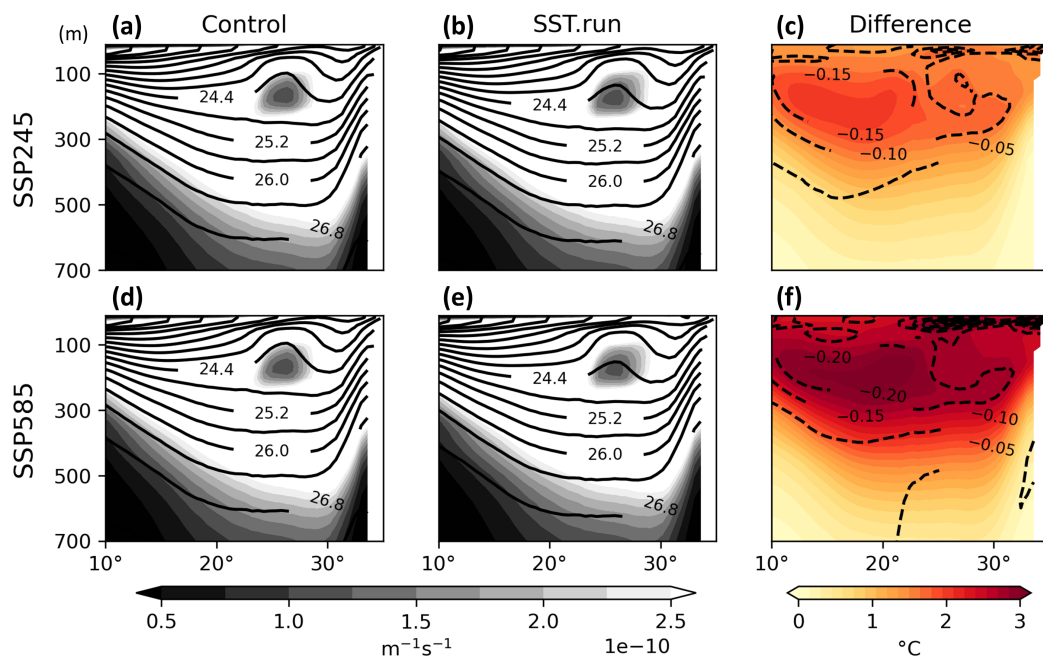

Figure 4.5: Same as Figure 4.4 but for the P09 (137°E).
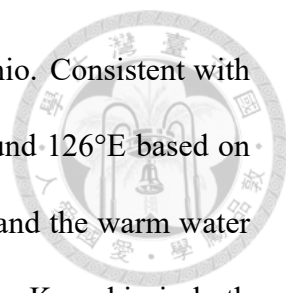
Figure 4.6 clarify the baroclinic changes across the ECS-Kuroshio. Consistent with the findings of CMIP6 (Figure 3.14), the Kuroshio is located at around 126°E based on the location of high mean temperature (Figure 4.6 (a), (b), (d), (e)), and the warm water changes distribution in the SST run occur primarily to the east of the Kuroshio in both scenarios(Figure 4.6 (c), (f)). The warm water is located particularly at a subsurface depths ranging from approximately 200 to 300 m. This depth is consistent with the SST-induced changes in meridional transport, as shown in Figure 4.3 (b). Besides, we have confirmed that the layer of no motion remains nearly unchanged across all experiments (Figure 4.3 (a)). Therefore, based on the thermal wind relation below, an increase in the zonal density gradient will enhance the northward geostrophic current.

$$\frac{\partial v}{\partial z} = -\frac{g}{\rho f}\frac{\partial \rho}{\partial x} \tag{4.1}$$

Although the magnitude of ocean warming significantly differs under different scenarios, the overall pattern of density change remains similar, suggesting a consistent zonal density gradient. Consequently, the differences in Kuroshio changes between two surface warming scenarios are minimal. Note that although our TIMCOM experiment exhibits a greater temperature change, the associated density change is relatively small compared to the results from CMIP6 (Figure 3.12, 3.13 and 3.14 (c), (f)). This discrepancy arises because we did not constraint the salinity flux. The intensification of the warm SST leads to increased evaporation, resulting in higher salinity levels that partially compensate the density change.

Figure 4.6: Vertical cross section along the zonal profile of the ECS-Kuroshio (26.75°N). The mean potential density (contour) and potential temperature (shading) in (a) SSP245.ctl and (b) SSP245.sst. (c) The difference between (b) SSP245.sst and (a) SSP245.ctl. (d, e, f) Same as (a, b, c) but for SSP5-8.5 scenario.
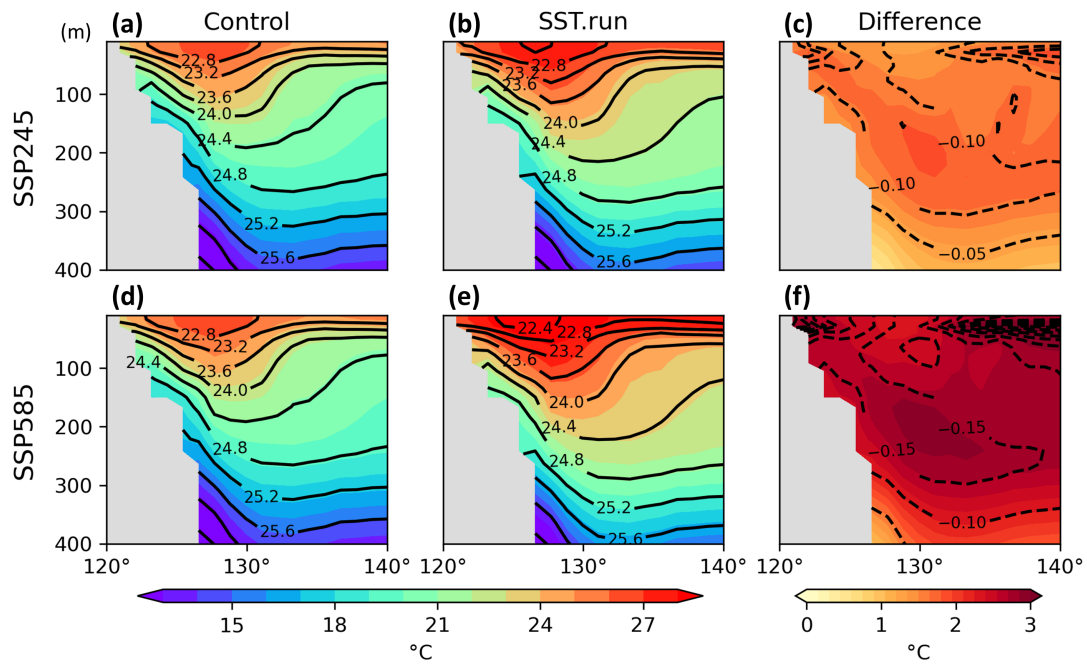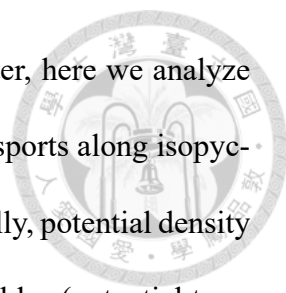
To clarify a clearer relationship between STMW and warm water, here we analyze variables at the same potential density layer because the STMW transports along isopycnal. We convert data from z-coordinate to isopycnal coordinate. Initially, potential density was computed in z-coordinate, followed by the interpolation of variables (potential temperature and PV) to isopycnal levels with a 0.1 kg/m^3 interval. Finally, isopycnal levels are chosen to determine the temperature difference between the SST sensitivity runs and the control runs. Because the density changes with sea water warming, different isopycnal levels are selected between these two runs, referring to (Wang et al., 2013). Base on the temperature change profile (Figure 4.4 and 4.5 (c), (f)), the density change at the location of STMW and warm water is approximately −0.1 (−0.2) kg/m^3 in SSP2-4.5 (SSP5-8.5) scenario. Therefore, the isopycnal in the SST run is chosen to be 0.1 (0.2) kg/m^3 lighter than that of the control run in each set of isopycnal.

Two different sets of isopycnal are chosen in each scenario (Figure 4.7). The low PV in the control runs (contour) indicates the location and pathway of STMW. The STMW subducts near the outcrop region of the KET and subsequently advects southeast to southwest along isopycnals (Hanawa and Talley, 2001; Xie et al., 2011). The warm sea water pattern corresponds to the low PV region in all different isopycnals and scenarios, demonstrating that the warm water from the sea surface indeed generates and transports along with the STMW. Besides, in shallower layers with densities of 24.8 / 24.7 kg/m^3 and 24.8 / 24.6 kg/m^3 in SSP2-4.5 and SSP5-8.5 scenario, respectively, the STMW propagates more directly southward (Figure 4.7 (b), (d)). Hence, the STMW on shallower layers are closer to the east of Kuroshio, allow the warm water to more effectively tilt the isopycnals across the Kuroshio and enhance the meridional velocity.
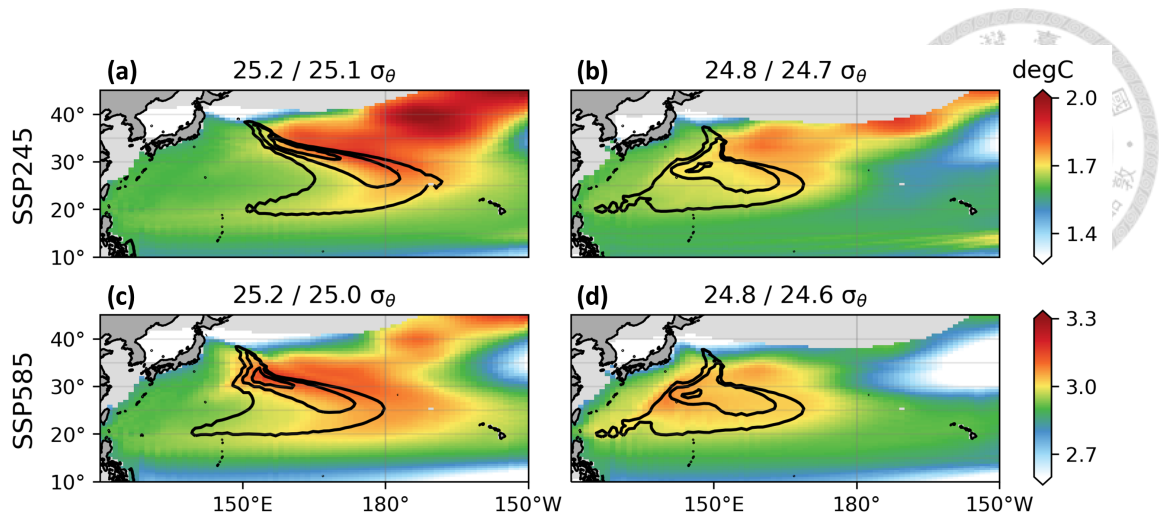
Figure 4.7: (a) Potential vorticity along 25.2 kg/m^3 isopycnals in SSP245.ctl (contour) and potential temperature change between SSP245.sst and SSP245.ctl along 25.1 kg/m^3 and 25.2 kg/m^3 isopycnals, respectively (shading). (b) Same as (a) but for SSP245.sst (SSP245.ctl) along 24.7 (24.8) kg/m^3 isopycnals. (c, d) Same as (a) but for SSP585.sst (SSP585.ctl) along 25.0 (25.2) kg/m^3 and 24.6 (24.8) kg/m^3 isopycnals, respectively.

In conclusion, our experiments demonstrate that the surface heating dominates the Kuroshio enhancement within the upper 300 m. The STMW subducts along with the warm water in the KET region and transports towards the east of the Kuroshio, resulting in a more inclined isopycnal across the Kuroshio and an increase in the northward velocity according to the thermal wind balance. Below a depth of 300 m, the signal of warm STMW diminishes, and wind changes become the primary factor of the Kuroshio's decline. Hence, this explain why the ECS-Kuroshio exhibits a baroclinic change in the LR ensemble of CMIP6. Furthermore, our analysis indicates that the response of the Kuroshio is more sensitive to the wind change, suggesting that a dominant factor of the model simulation for the Kuroshio change may shift depending on the magnitude of wind variation.

47

Chapter 5   Discussion

This study aims to investigate the fundamental differences causing the Kuroshio changes among future scenario simulations. In order to specify the underlying physical mechanisms, we also examine the role of individual forcing in global LR models. According to the CMIP6 ensembles, the Kuroshio change in the SSP5-8.5 simulations depends on different latitude, depth, variables, and either model resolutions (Table 5.1).

The KE of ECS-Kuroshio in the LR simulation exhibits an increase in the upper 300 m but a decrease in the upper 1000 m in the CMIP6 ensemble. Our isopycnal analysis in the LR sensitivity experiments have clarified that the baroclinic change is primarily influenced by the warm STMW (Figure 4.7). In the future scenario, the warm sea surface subducts with the STMW through mixing and transport with the wind-driven subtropical gyre. The warm STMW contributes to elevated sea water temperatures in the east of the Kuroshio, leading to an increased isopycnal slope across the Kuroshio and strengthening the Kuroshio. The intensification is more pronounced in the upper layer and surpasses the reduction caused by wind effects in both the SSP2-4.5 and SSP5-8.5 scenarios. Below a depth of around 300 m, the influence of the warm STMW diminishes, and the Kuroshio change is dominated by the effect of wind change. Note that the Kuroshio change is more sensitive to the magnitude of wind change compared to the SST warming change. However, Chen et al. (2019) and Peng et al. (2022) has shown that SST is the dominant factor throughout the entire water column, including the decrease in Kuroshio velocity

49

between 400 to 1200 m depth. This could potentially be because of the different numerical settings employed on the sea floor. A more careful inspection is needed.

Additionally, we also found differences in the KE and transport changes in the upper layer of the ECS-Kuroshio in CMIP6 LR ensemble. The differences can be attributed to the anti-cyclonic circulation change surrounding the Ryukyu Island chain (Figure 3.5). This results in an increase in the main axis of the Kuroshio's KE while the net transport across the circulation remains unchanged.

The contrasting tendency between the JP-Kuroshio and the ECS-Kuroshio in the CMIP6 upper 1000 m and the HR simulation's upper 300 m can be attributed to the expansion of the Hadley cell. This expansion leads to a poleward shift of zero for the WSC line, resulting in a reduction of negative WSC to the south of 30°N and an increased of negative WSC to the north. As a result, the JP-Kuroshio experiences enhancement while the ECS-Kuroshio undergoes weakening according to the Sverdrup theory. The Sverdrup relation depicted in Figure 3.10 and 3.11 further shows that the magnitude of the Kuroshio changes depending on the magnitude of WSC change across different ocean models. Note that only the KET in HR models have simulated a significant poleward shift in response to the Hadley cell expansion, possibly indicating the inadequate simulation of KET in the LR models. The wind driven mechanism is supported by Sakamoto et al. (2005), Cheon et al. (2012), etc.

However, in the upper 300 m, both Chen et al. (2019) and our LR experiments indicate that the dominant increase in KE, attributed to the warm SST, is not limited to the ECS-Kuroshio, but also along the south Japanese coast. The physical process could be

50

attributed to the warm STMW similar to the ECS-Kuroshio mentioned above, or it could be influenced by strengthened ocean stratification that accelerates velocity through PV conservation (Zhang et al., 2017). It is noteworthy that the Sverdrup relation shown in Figure 3.11 suggests that the JP-Kuroshio change is more sensitive to the WSC change in the HR simulations. Furthermore, the vertical profiles (Figure 3.12 to 3.14) demonstrate that the warm water, along with STMW, is not significant in the HR, which may affect the dominant mechanism. Therefore, further investigation is required to determine whether the STMW primarily enhances the Kuroshio in the HR.

Table 5.1: Summary of different part of Kuroshio change in CMIP6 ensembles.

Upper 300 m	Low Resolution	High Resolution
JP-Kuroshio	enhanced	enhanced dramatically, poleward
ECS-Kuroshio	KE: enhanced	reduced
	Sv: no changed	

Upper 1000 m	Low Resolution	High Resolution
JP-Kuroshio	enhanced	enhanced dramatically, poleward
ECS-Kuroshio	reduced	

51

References

Ambe, D., Imawaki, S., Uchida, H., and Ichikawa, K. (2004). Estimating the kuroshio axis south of japan using combination of satellite altimetry and drifting buoys. *Journal of Oceanography*, 60:375–382.

Chang, M.-H., Jan, S., Mensah, V., Andres, M., Rainville, L., Yang, Y. J., and Cheng, Y.-H. (2018). Zonal migration and transport variations of the kuroshio east of taiwan induced by eddy impingements. *Deep Sea Research Part I: Oceanographic Research Papers*, 131:1–15.

Chen, C., Wang, G., Xie, S.-P., and Liu, W. (2019). Why does global warming weaken the gulf stream but intensify the kuroshio? *Journal of Climate*, 32(21):7437–7451.

Cheon, W. G., Park, Y.-G., Yeh, S.-W., and Kim, B.-M. (2012). Atmospheric impact on the northwestern pacific under a global warming scenario. *Geophysical research letters*, 39(16).

Choi, B.-H., Kim, D.-H., and Kim, J.-W. (2002). Regional responses of climate in the northwestern pacific ocean to gradual global warming for a co2 quadrupling. *Journal of the Meteorological Society of Japan. Ser. II*, 80(6):1427–1442.

Davis, N. A. and Birner, T. (2022). Eddy-mediated hadley cell expansion due to ax-

isymmetric angular momentum adjustment to greenhouse gas forcings. *Journal of the Atmospheric Sciences*, 79(1):141–159.
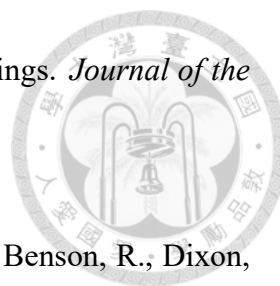
Delworth, T. L., Rosati, A., Anderson, W., Adcroft, A. J., Balaji, V., Benson, R., Dixon, K., Griffies, S. M., Lee, H.-C., Pacanowski, R. C., et al. (2012). Simulated climate and climate change in the gfdl cm2. 5 high-resolution coupled climate model. *Journal of Climate*, 25(8):2755–2781.

Douglass, E. M., Kwon, Y.-O., and Jayne, S. R. (2013). A comparison of north pacific and north atlantic subtropical mode waters in a climatologically-forced model. *Deep Sea Research Part II: Topical Studies in Oceanography*, 91:139–151.

Gent, P. R. and Mcwilliams, J. C. (1990). Isopycnal mixing in ocean circulation models. *Journal of Physical Oceanography*, 20(1):150–155.

Hallberg, R. (2013). Using a resolution function to regulate parameterizations of oceanic mesoscale eddy effects. *Ocean Modelling*, 72:92–103.

Hanawa, K. and Talley, L. D. (2001). Mode waters. In *International Geophysics*, volume 77, pages 373–386. Elsevier.

Hu, S., Sprintall, J., Guan, C., McPhaden, M. J., Wang, F., Hu, D., and Cai, W. (2020). Deep-reaching acceleration of global mean ocean circulation over the past two decades. *Science advances*, 6(6):eaax7727.

Hunke, E., Lipscomb, W., Jones, P., Turner, A., Jeffery, N., and Elliott, S. (2017). Cice, the los alamos sea ice model. Technical report, Los Alamos National Lab.(LANL), Los Alamos, NM (United States).

Hurlburt, H. E., Wallcraft, A. J., Schmitz Jr, W. J., Hogan, P. J., and Metzger, E. J. (1996). Dynamics of the kuroshio/oyashio current system using eddy-resolving models of the north pacific ocean. *Journal of Geophysical Research: Oceans*, 101(C1):941–976.

Jayne, S. R., Hogg, N. G., and Malanotte-Rizzoli, P. (1996). Recirculation gyres forced by a beta-plane jet. *Journal of physical oceanography*, 26(4):492–504.

Kida, S., Mitsudera, H., Aoki, S., Guo, X., Ito, S.-i., Kobashi, F., Komori, N., Kubokawa, A., Miyama, T., Morie, R., et al. (2016). Oceanic fronts and jets around japan: a review. *"Hot Spots" in the Climate System: New Developments in the Extratropical Ocean-Atmosphere Interaction Research*, pages 1–30.

Kirtman, B. P., Bitz, C., Bryan, F., Collins, W., Dennis, J., Hearn, N., Kinter, J. L., Loft, R., Rousset, C., Siqueira, L., et al. (2012). Impact of ocean model resolution on ccsm climate simulations. *Climate dynamics*, 39:1303–1328.

Large, W. and Yeager, S. (2009). The global climatology of an interannually varying air–sea flux data set. *Climate dynamics*, 33:341–364.

Large, W. G., McWilliams, J. C., and Doney, S. C. (1994). Oceanic vertical mixing: A review and a model with a nonlocal boundary layer parameterization. *Reviews of geophysics*, 32(4):363–403.

Lu, J., Vecchi, G. A., and Reichler, T. (2007). Expansion of the hadley cell under global warming. *Geophysical Research Letters*, 34(6).

Ma, X., Jing, Z., Chang, P., Liu, X., Montuoro, R., Small, R. J., Bryan, F. O., Greatbatch, R. J., Brandt, P., Wu, D., et al. (2016). Western boundary currents regulated by interaction between ocean eddies and the atmosphere. *Nature*, 535(7613):533–537.

Marshall, J. and Nurser, G. (1986). Steady, free circulation in a stratified quasi-geostrophic ocean. *Journal of physical oceanography*, 16(11):1799–1813.

Martínez-Moreno, J., Hogg, A. M., England, M. H., Constantinou, N. C., Kiss, A. E., and Morrison, A. K. (2021). Global changes in oceanic mesoscale currents over the satellite altimetry record. *Nature Climate Change*, 11(5):397–403.

Peng, Q., Xie, S.-P., Wang, D., Huang, R. X., Chen, G., Shu, Y., Shi, J.-R., and Liu, W. (2022). Surface warming–induced global acceleration of upper ocean currents. *Science Advances*, 8(16):eabj8394.

Qiu, B. and Chen, S. (2005). Variability of the kuroshio extension jet, recirculation gyre, and mesoscale eddies on decadal time scales. *Journal of Physical Oceanography*, 35(11):2090–2103.

Qiu, B. and Chen, S. (2010). Eddy-mean flow interaction in the decadally modulating kuroshio extension system. *Deep Sea Research Part II: Topical Studies in Oceanography*, 57(13-14):1098–1110.

Qiu, B., Chen, S., Wu, L., and Kida, S. (2015). Wind-versus eddy-forced regional sea level trends and variability in the north pacific ocean. *Journal of Climate*, 28(4):1561–1577.

Sakamoto, T. T., Hasumi, H., Ishii, M., Emori, S., Suzuki, T., Nishimura, T., and Sumi, A. (2005). Responses of the kuroshio and the kuroshio extension to global warming in a high-resolution climate model. *Geophysical Research Letters*, 32(14).

Sasaki, Y. N. and Umeda, C. (2021). Rapid warming of sea surface temperature along the kuroshio and the china coast in the east china sea during the twentieth century. *Journal of Climate*, 34(12):4803–4815.

Sato, Y., Yukimoto, S., Tsujino, H., Ishizaki, H., and Noda, A. (2006). Response of north pacific ocean circulation in a kuroshio-resolving ocean model to an arctic oscillation (ao)-like change in northern hemisphere atmospheric circulation due to greenhouse-gas forcing. *Journal of the Meteorological Society of Japan. Ser. II*, 84(2):295–309.

Seager, R., Kushnir, Y., Naik, N. H., Cane, M. A., and Miller, J. (2001). Wind-driven shifts in the latitude of the kuroshio–oyashio extension and generation of sst anomalies on decadal timescales. *Journal of Climate*, 14(22):4249–4265.

Sen Gupta, A., Stellema, A., Pontes, G. M., Taschetto, A. S., Vergés, A., and Rossi, V. (2021). Future changes to the upper ocean western boundary currents across two generations of climate models. *Scientific Reports*, 11(1):1–12.

Small, R. d., deSzoeke, S. P., Xie, S., O'neill, L., Seo, H., Song, Q., Cornillon, P., Spall, M., and Minobe, S. (2008). Air–sea interaction over ocean fronts and eddies. *Dynamics of Atmospheres and Oceans*, 45(3-4):274–319.

Tseng, Y.-h., Lin, H., Chen, H.-c., Thompson, K., Bentsen, M., Böning, C. W., Bozec, A., Cassou, C., Chassignet, E., Chow, C. H., et al. (2016). North and equatorial pacific ocean circulation in the core-ii hindcast simulations. *Ocean Modelling*, 104:143–170.

Tseng, Y.-H., Shen, M.-L., Jan, S., Dietrich, D. E., and Chiang, C.-P. (2012). Validation of the kuroshio current system in the dual-domain pacific ocean model framework. *Progress in Oceanography*, 105:102–124.

Tseng, Y.-H., Tsao, S.-E., Kuo, Y.-C., and Tsai, J.-Y. (2022). Timcom model datasets for the cmip6 ocean model intercomparison project. *Ocean Modelling*, 179:102109.

57

Tsubouchi, T., Suga, T., and Hanawa, K. (2016). Comparison study of subtropical mode waters in the world ocean. *Frontiers in Marine Science*, 3:270.
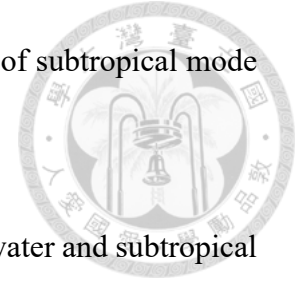
Wang, L., Liu, Q., Xu, L., and Xie, S.-P. (2013). Response of mode water and subtropical countercurrent to greenhouse gas and aerosol forcing in the north pacific. *Journal of Ocean University of China*, 12:222–229.

Wang, Y.-C., Hsu, H.-H., Chen, C.-A., Tseng, W.-L., Hsu, P.-C., Lin, C.-W., Chen, Y.-L., Jiang, L.-C., Lee, Y.-C., Liang, H.-C., et al. (2021). Performance of the taiwan earth system model in simulating climate variability compared with observations and cmip6 model simulations. *Journal of Advances in Modeling Earth Systems*, 13(7):e2020MS002353.
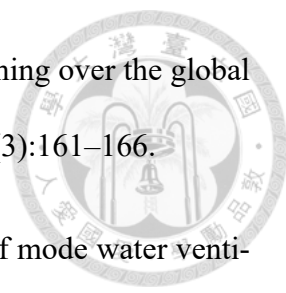
Wang, Y.-L., Wu, C.-R., and Chao, S.-Y. (2016). Warming and weakening trends of the kuroshio during 1993–2013. *Geophysical Research Letters*, 43(17):9200–9207.

Waterman, S. and Jayne, S. R. (2011). Eddy-mean flow interactions in the along-stream development of a western boundary current jet: An idealized model study. *Journal of Physical Oceanography*, 41(4):682–707.

Williams, P. D. (2009). A proposed modification to the robert–asselin time filter. *Monthly Weather Review*, 137(8):2538–2546.

Wu, B., Lin, X., and Yu, L. (2021). Poleward shift of the kuroshio extension front and its impact on the north pacific subtropical mode water in the recent decades. *Journal of Physical Oceanography*, 51(2):457–474.

Wu, L., Cai, W., Zhang, L., Nakamura, H., Timmermann, A., Joyce, T., McPhaden, M. J.,

Alexander, M., Qiu, B., Visbeck, M., et al. (2012). Enhanced warming over the global subtropical western boundary currents. *Nature Climate Change*, 2(3):161–166.

Xie, S.-P., Xu, L., Liu, Q., and Kobashi, F. (2011). Dynamical role of mode water ventilation in decadal variability in the central subtropical gyre of the north pacific. *Journal of Climate*, 24(4):1212–1225.

Yamanaka, G., Nakano, H., Sakamoto, K., Toyoda, T., Urakawa, L. S., Nishikawa, S., Wakamatsu, T., Tsujino, H., and Ishikawa, Y. (2021). Projected climate change in the western north pacific at the end of the 21st century from ensemble simulations with a high-resolution regional ocean model. *Journal of oceanography*, 77:539–560.

Yang, H., Lohmann, G., Wei, W., Dima, M., Ionita, M., and Liu, J. (2016). Intensification and poleward shift of subtropical western boundary currents in a warming climate. *Journal of Geophysical Research: Oceans*, 121(7):4928–4945.

Young, C.-C., Liang, Y.-C., Tseng, Y.-H., and Chow, C.-H. (2014). Characteristics of the raw-filtered leapfrog time-stepping scheme in the ocean general circulation model. *Monthly Weather Review*, 142(1):434–447.

Zhang, X., Wang, Q., and Mu, M. (2017). The impact of global warming on kuroshio extension and its southern recirculation using cmip5 experiments with a high-resolution climate model miroc4h. *Theoretical and Applied Climatology*, 127:815–827.

Appendix A — Supplementary Figures
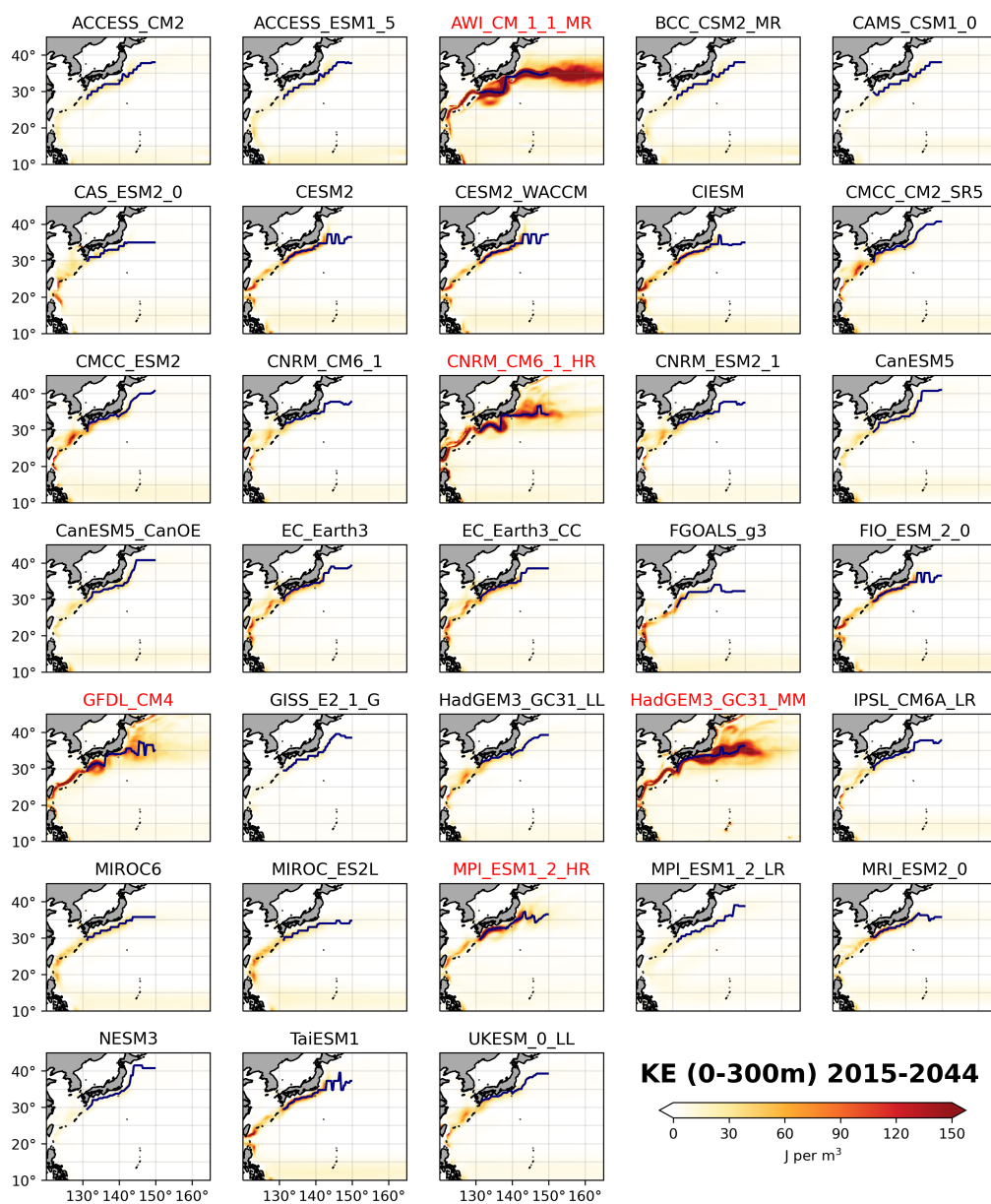
Figure A.1: The 2015-2044 mean of upper 300 m KE for each model. The blue lines represent the KET axis.
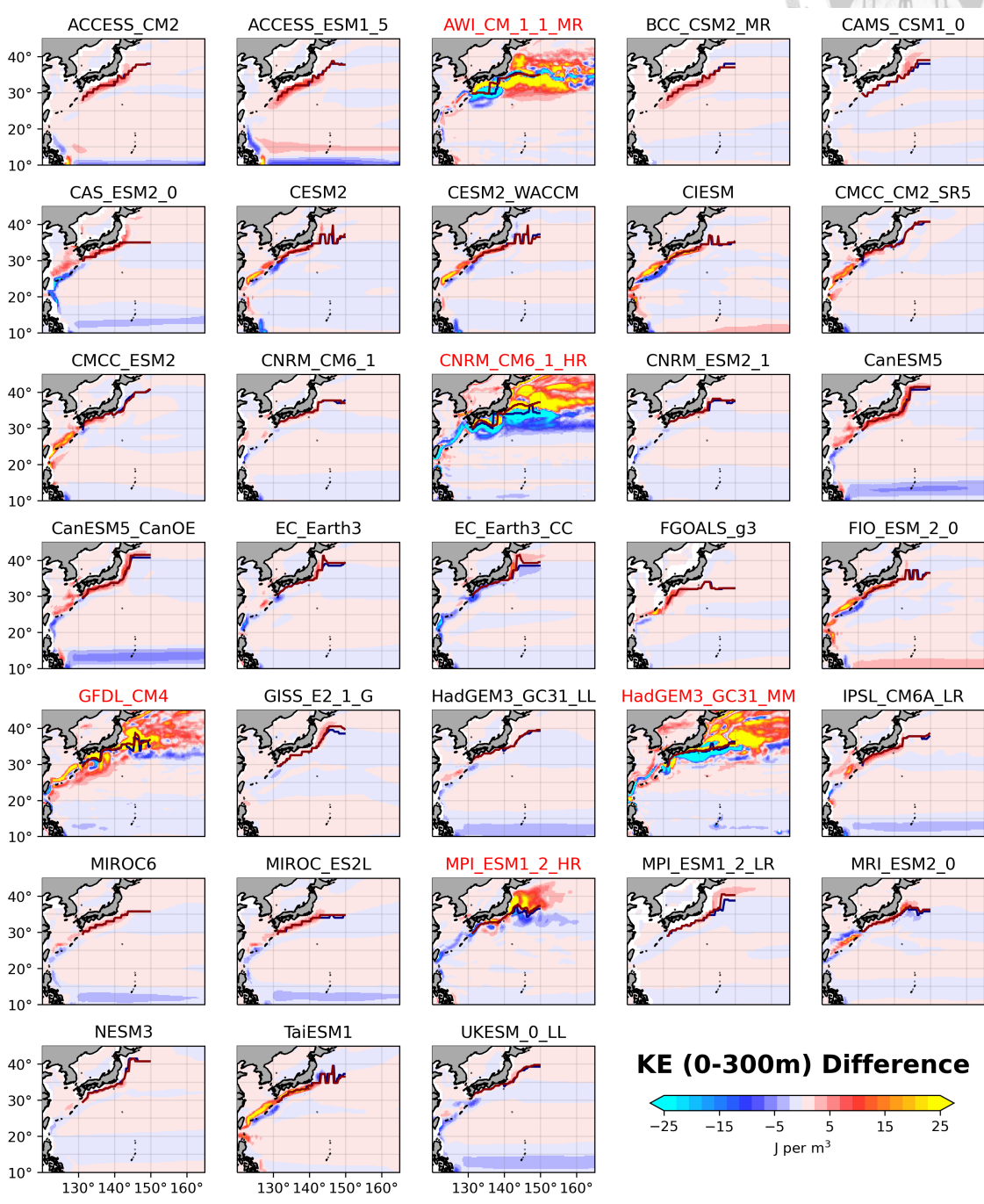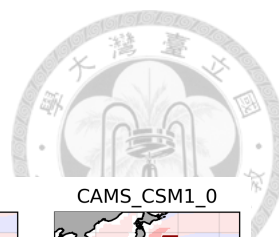
Figure A.2: The difference of upper 300 m KE between 2070-2099 and 2015-2044. The blue (red) line indicates the mean of the KE axis in 2015-2044 (2070-2099).
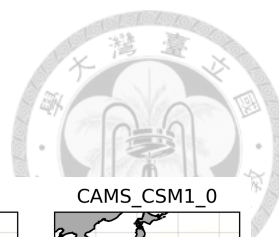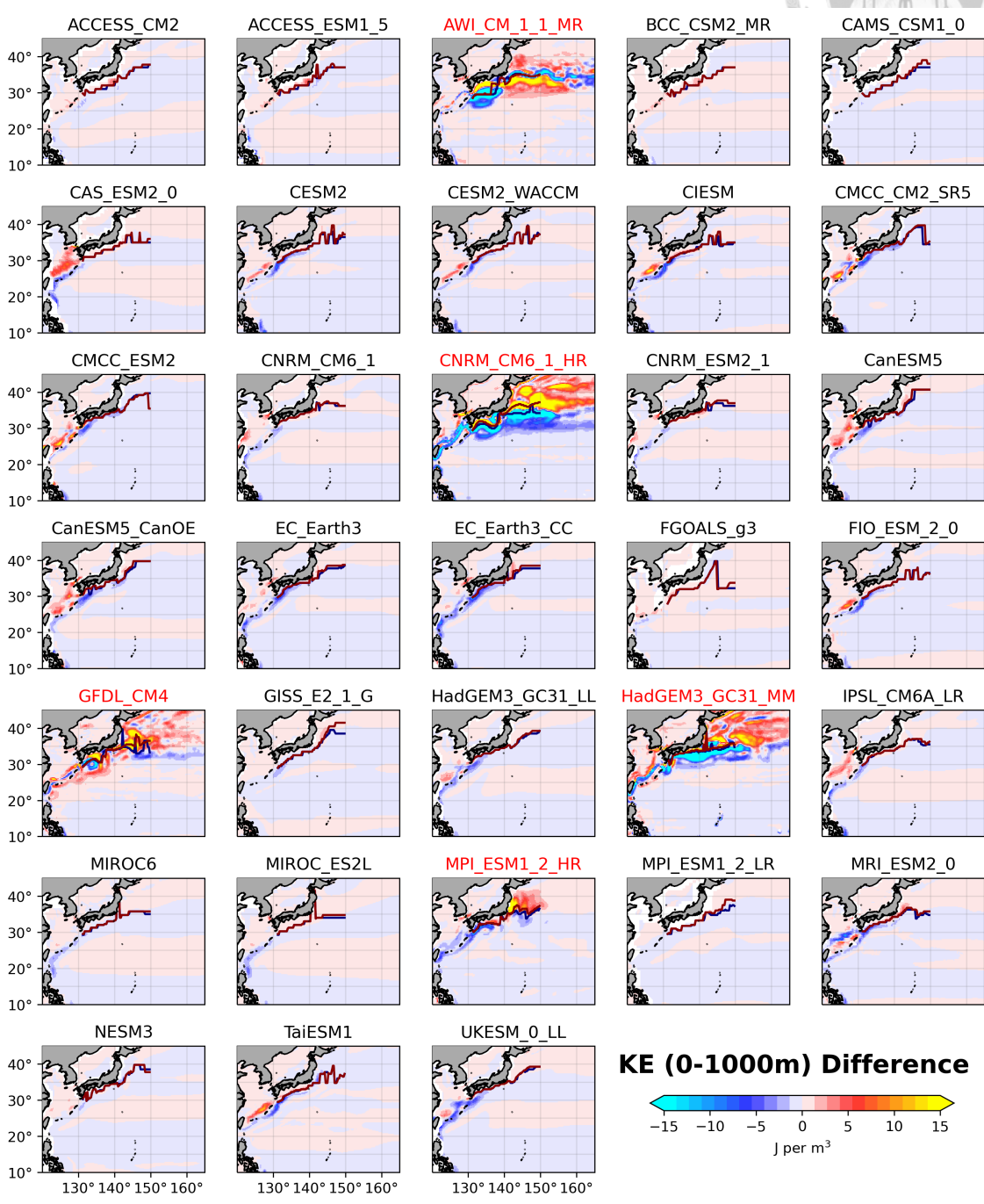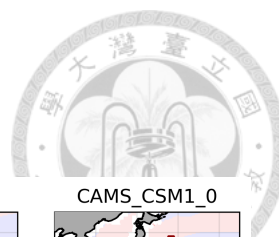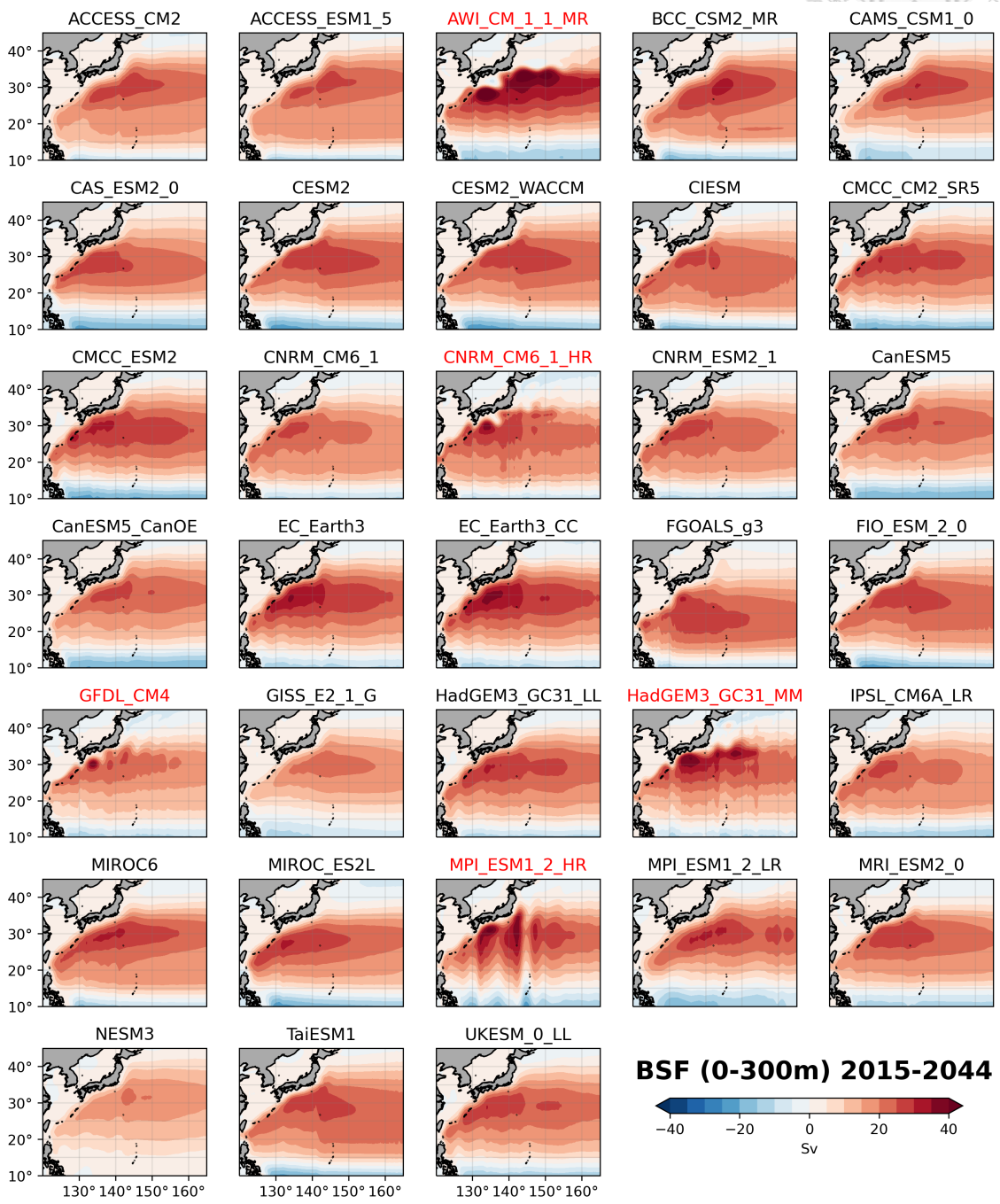
62
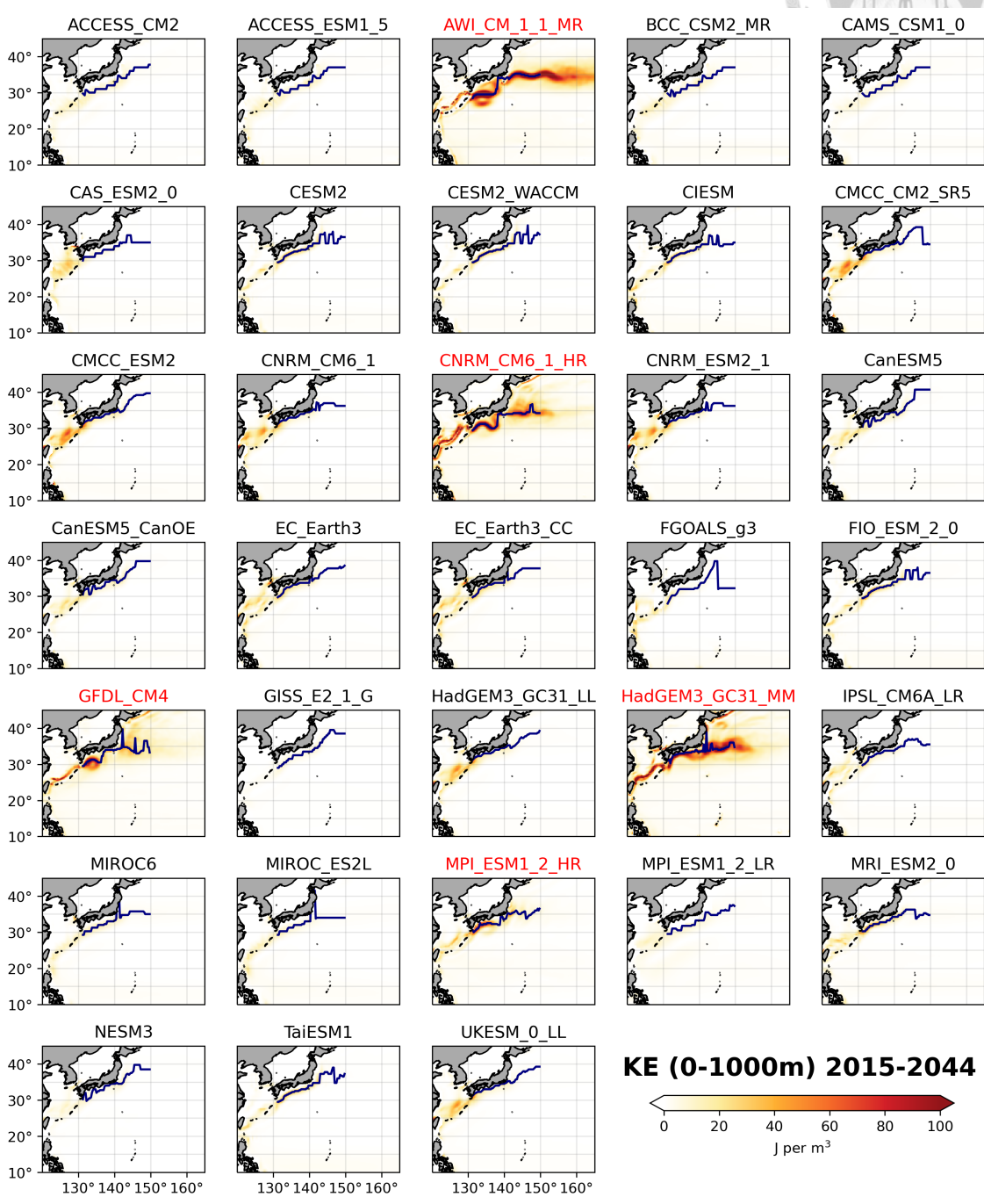
Figure A.3: The difference of upper 1000 m KE between 2070-2099 and 2015-2044. The blue lines represent the KET axis.

Figure A.4: The difference of upper 1000 m KE between 2070-2099 and 2015-2044. The blue (red) line indicates the mean of the KE axis in 2015-2044 (2070-2099).

Figure A.5: The 2015-2044 mean of upper 300 m BSF for each model.
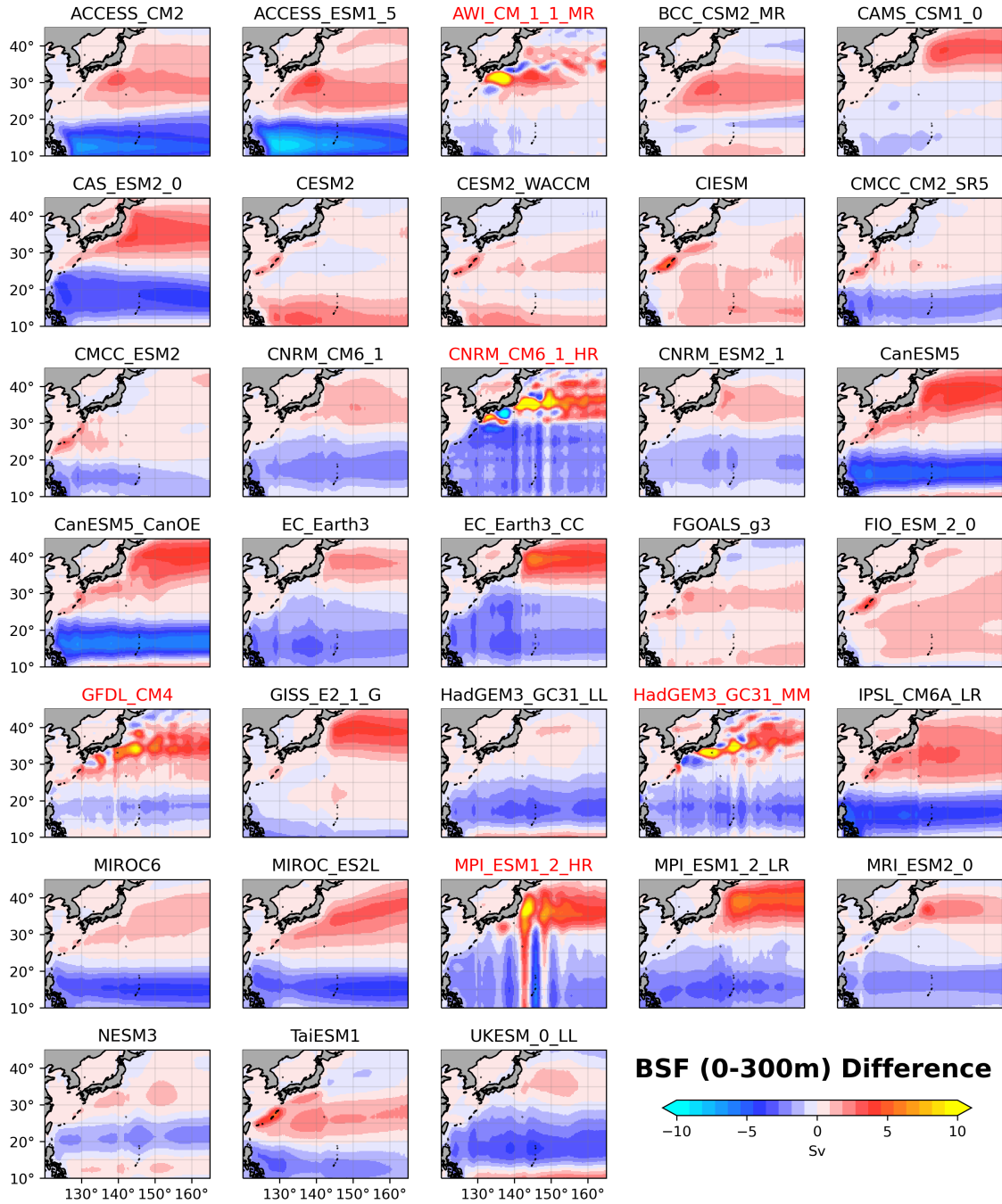
Figure A.6: The difference of upper 300 m BSF between 2070-2099 and 2015-2044.
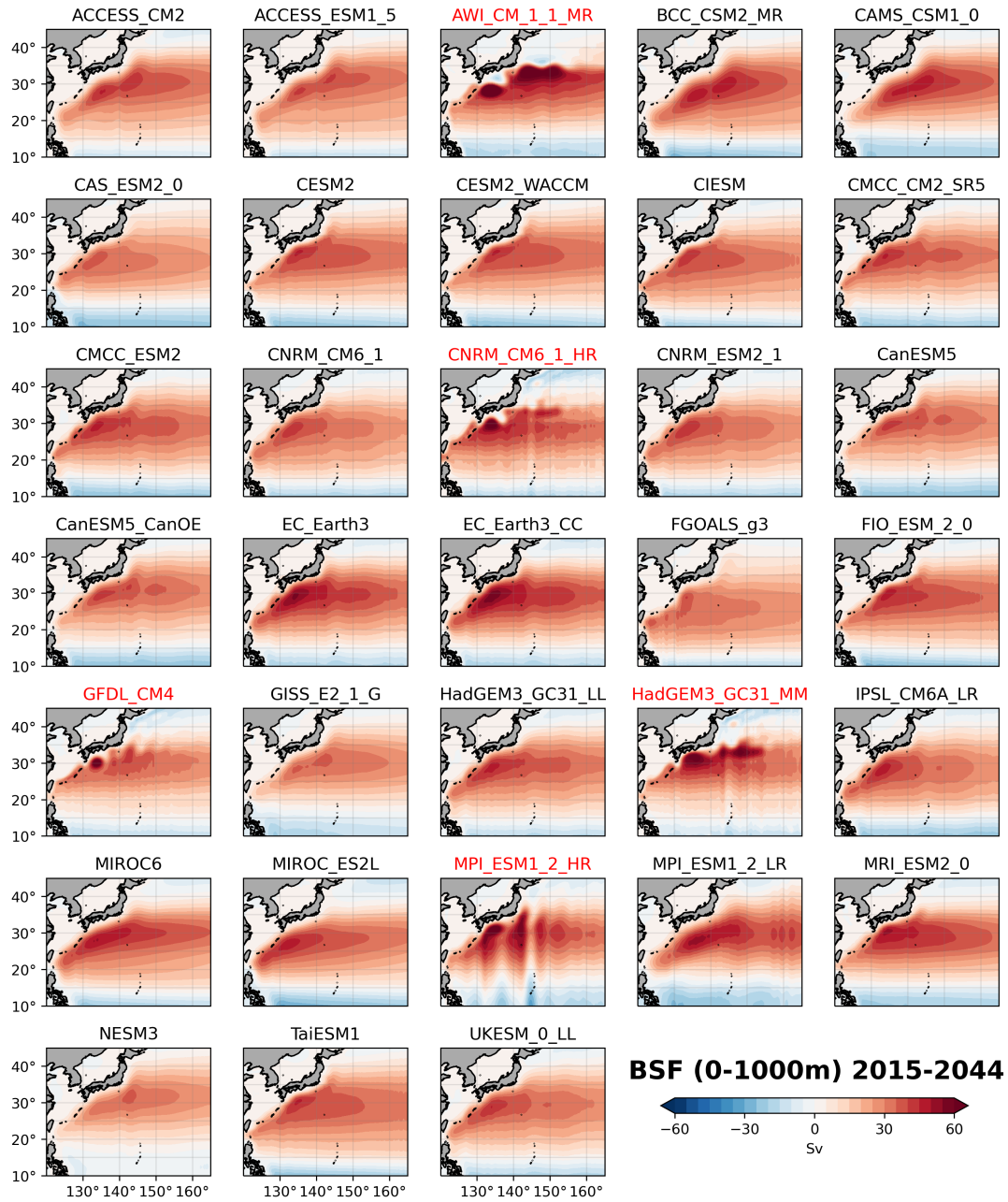
Figure A.7: The 2015-2044 mean of upper 1000 m BSF for each model.
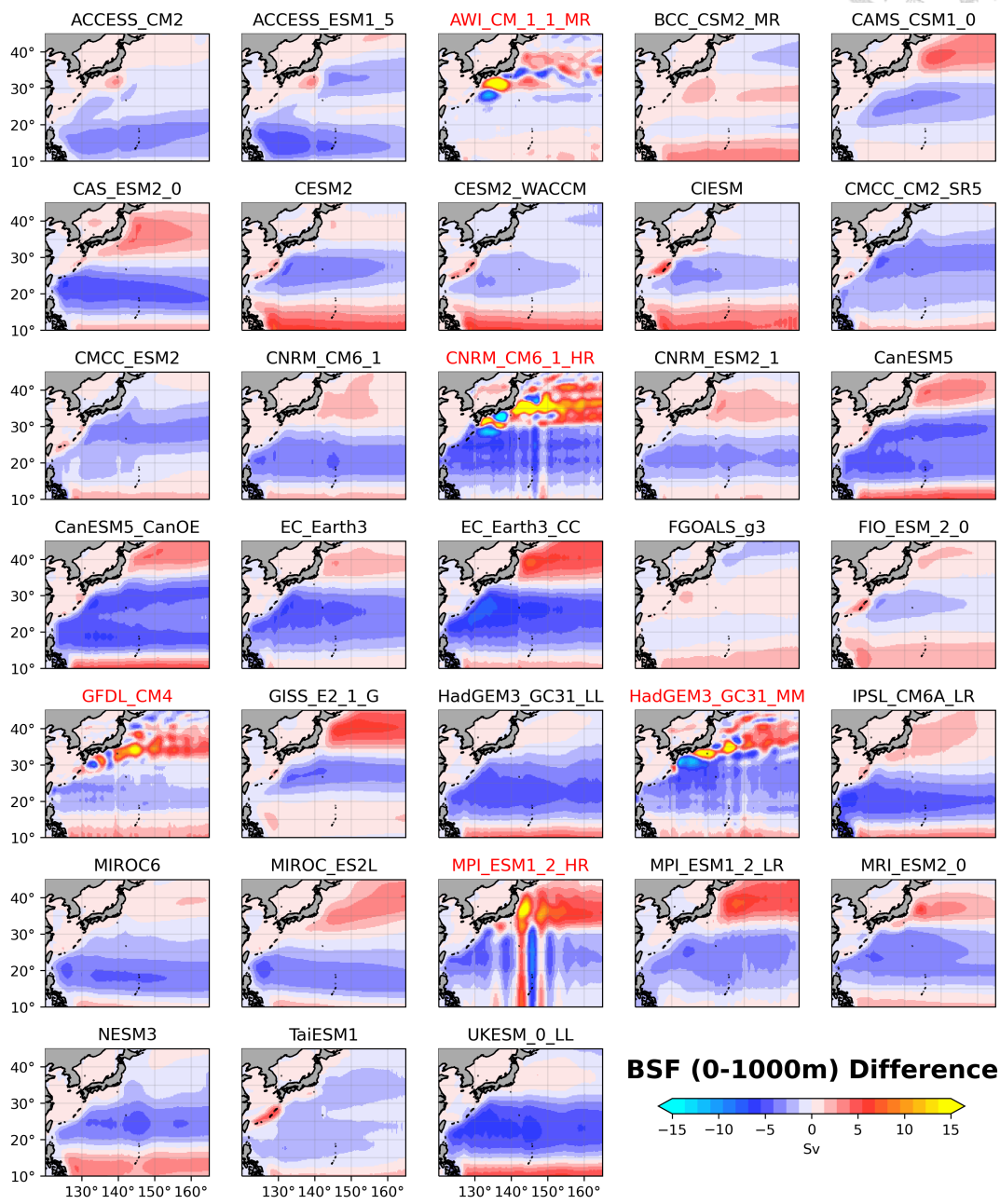
Figure A.8: The difference of upper 1000 m BSF between 2070-2099 and 2015-2044.
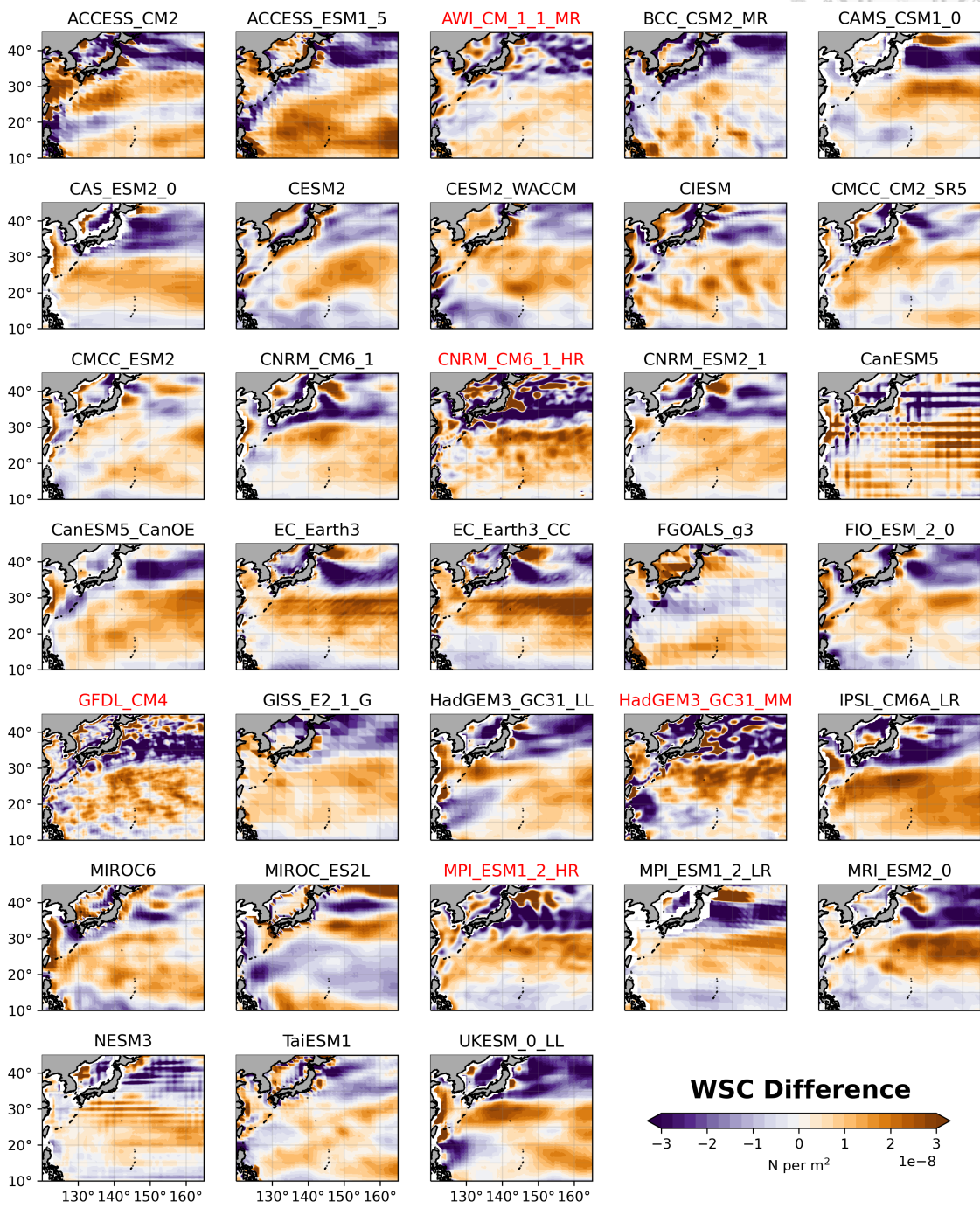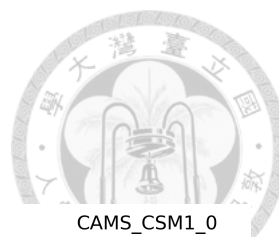
Figure A.9: The difference of WSC between 2070-2099 and 2015-2044.

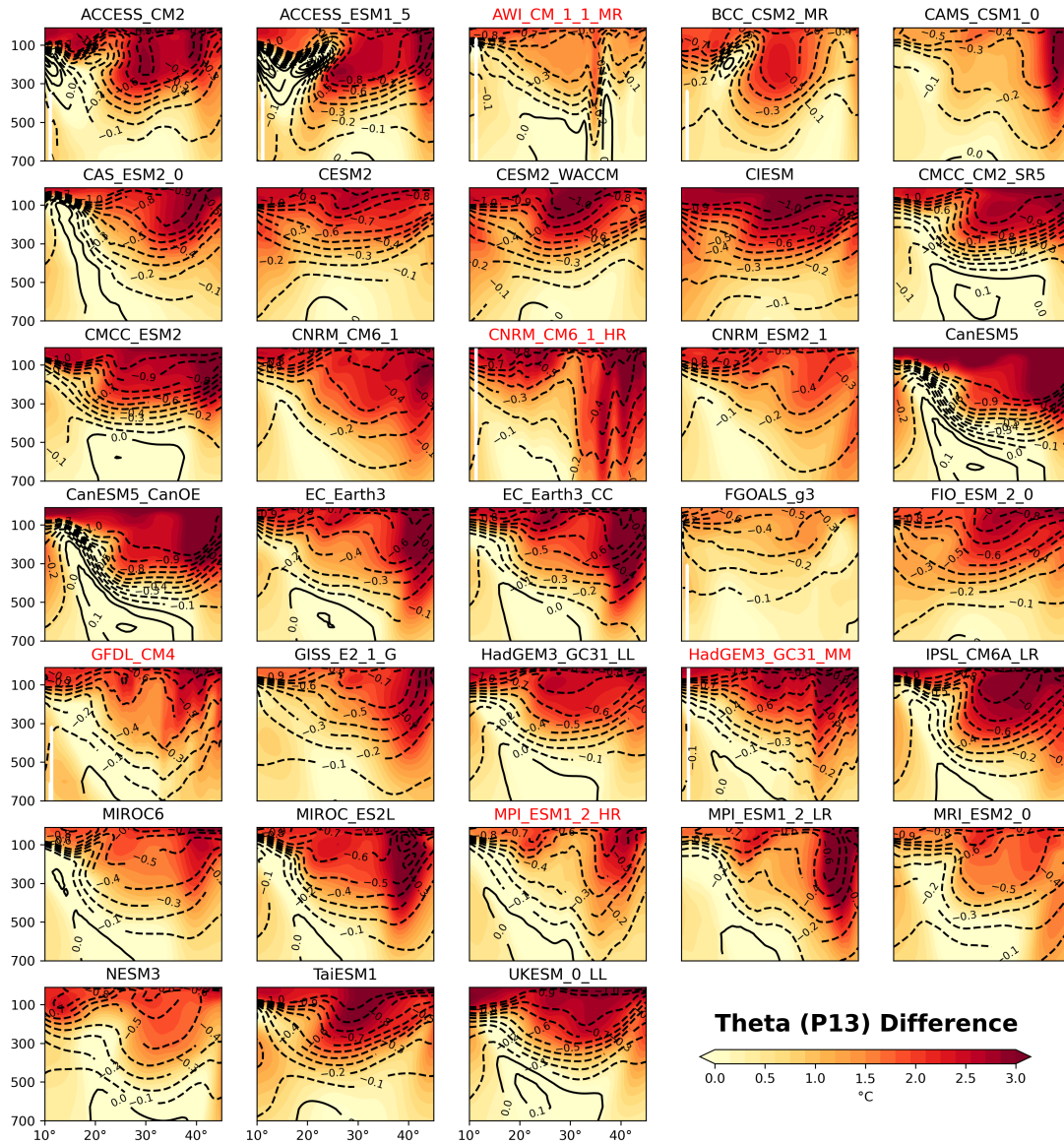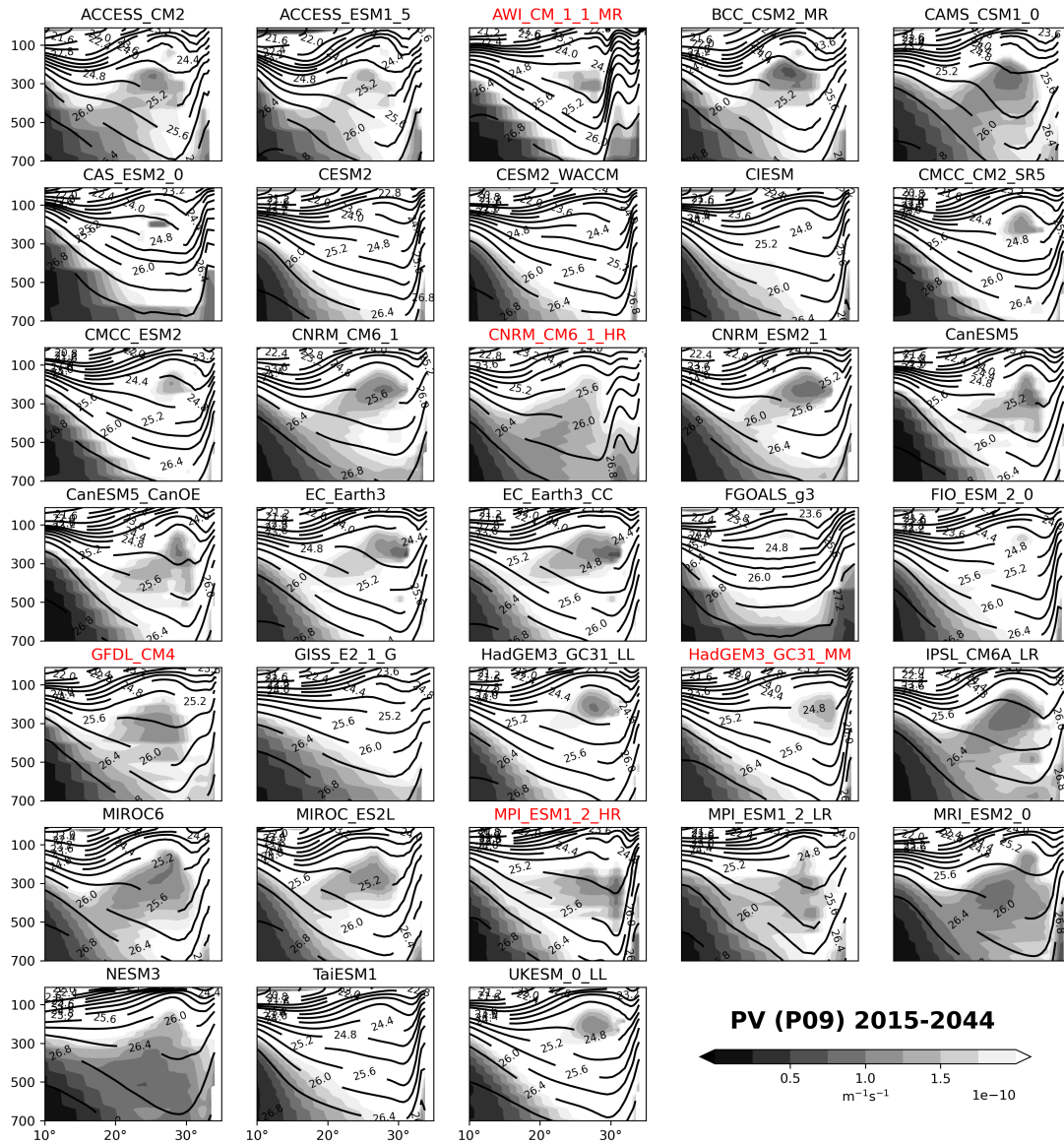Figure A.10: Vertical cross section along the P13 (165°E). The 2015-2044 mean of potential density (contour) and potential vorticity (shading) for each model.
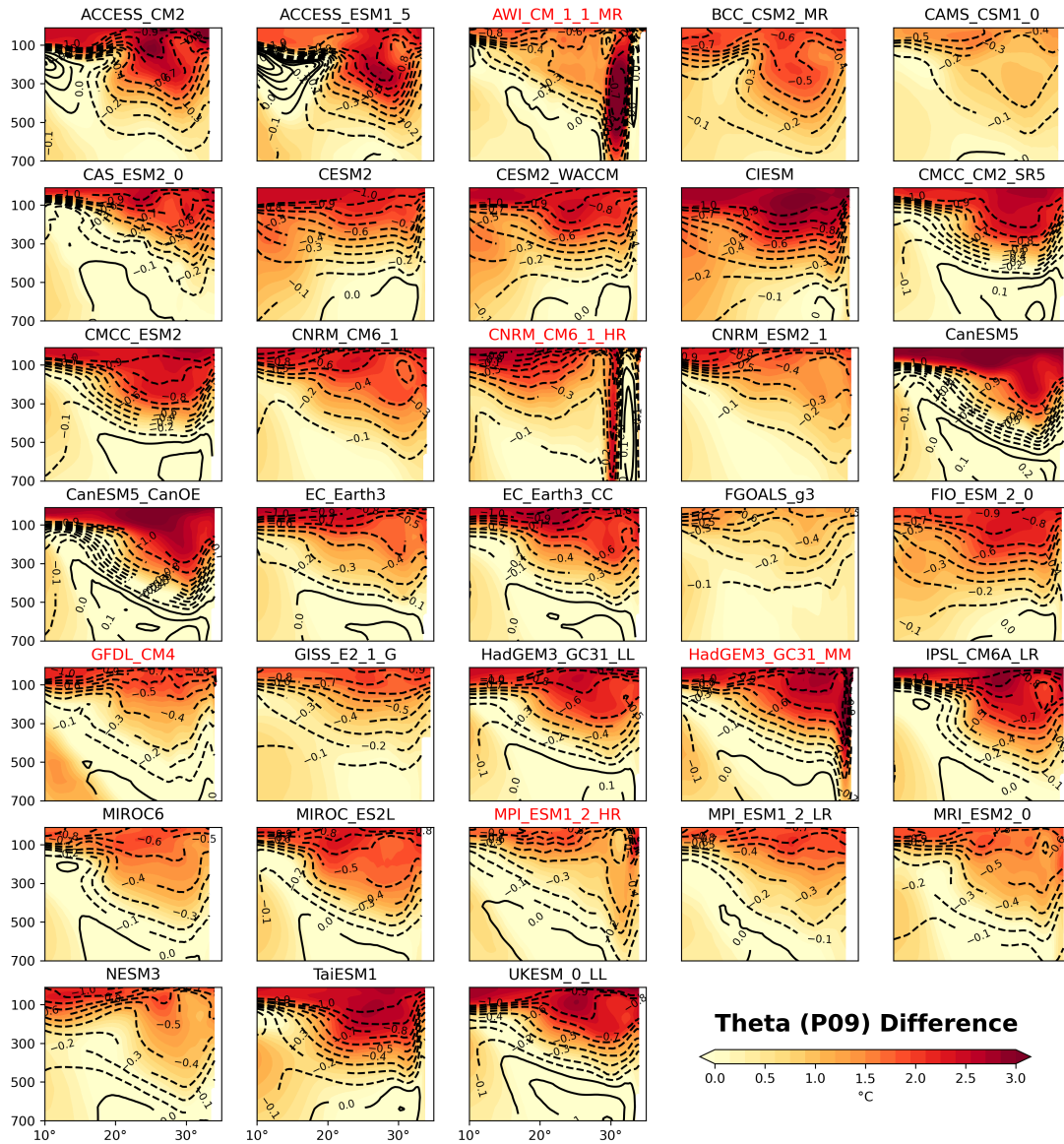
Figure A.11: Vertical cross section along the P13 (165°E). The difference of potential density (contour) and potential temperature (shading) between 2070-2099 and 2015-2044.
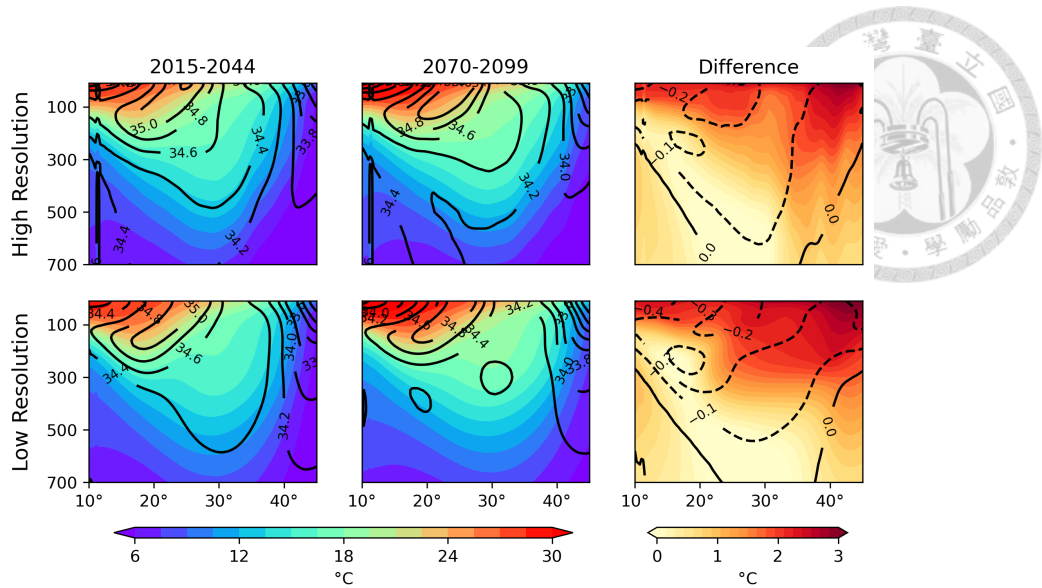
Figure A.12: Vertical cross section along the P09 (137°E). The 2015-2044 mean of potential density (contour) and potential vorticity (shading) for each model.

Figure A.13: Vertical cross section along the P09 (137°E). The difference of potential density (contour) and potential temperature (shading) between 2070-2099 and 2015-2044.

73

Figure A.14: Vertical cross section along the P13 (165°E). (a) The 2015-2044 mean of salinity (contour) and potential temperature (shading) for HR models. (b) Same as (a) but for 2070-2099. (c) The difference between (b) 2070-2099 and (a) 2015-2044. (d, e, f) Same as (a, b, c) but for LR models.
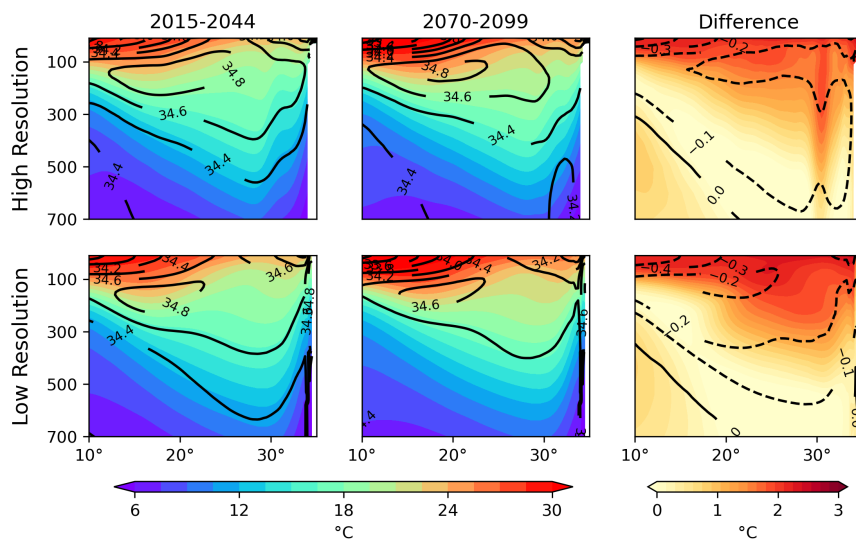

Figure A.15: Vertical cross section along the P09 (137°E). (a) The 2015-2044 mean of salinity (contour) and potential temperature (shading) for HR models. (b) Same as (a) but for 2070-2099. (c) The difference between (b) 2070-2099 and (a) 2015-2044. (d, e, f) Same as (a, b, c) but for LR models.
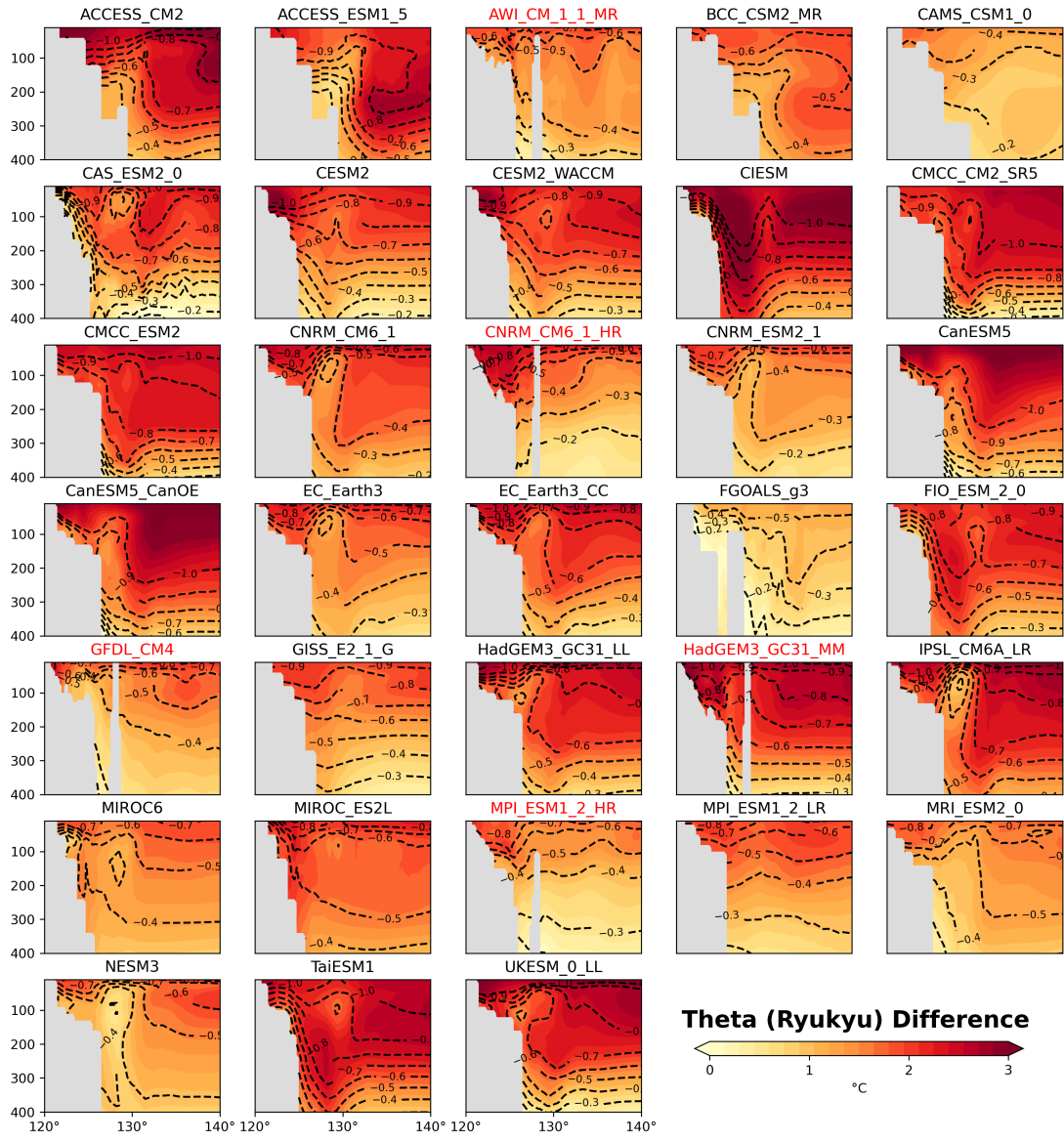
74

Figure A.16: Vertical cross section along the zonal profile of the ECS-Kuroshio (26.75°N). The difference of potential density (contour) and potential temperature (shading) between 2070-2099 and 2015-2044.
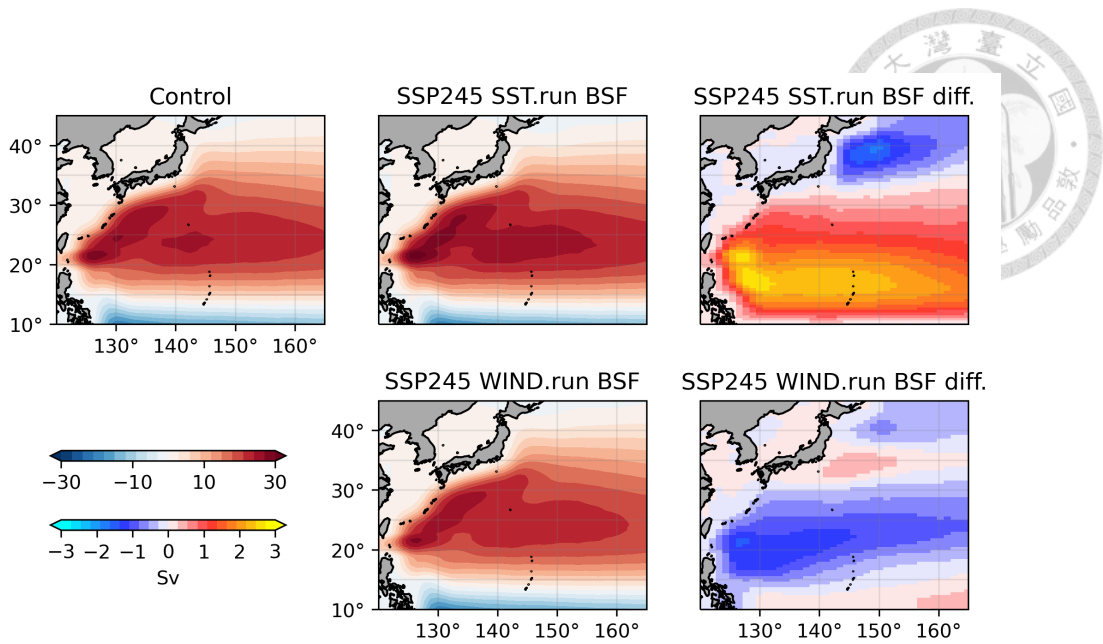
75

Figure A.17: The upper 300 m BSF in (a) SSP245.ctl and (b) SSP245.sst. (c) The difference between (b) SSP245.sst and (a) SSP245.ctl. (d, e) Same as (b, c) but for SSP245.wind.
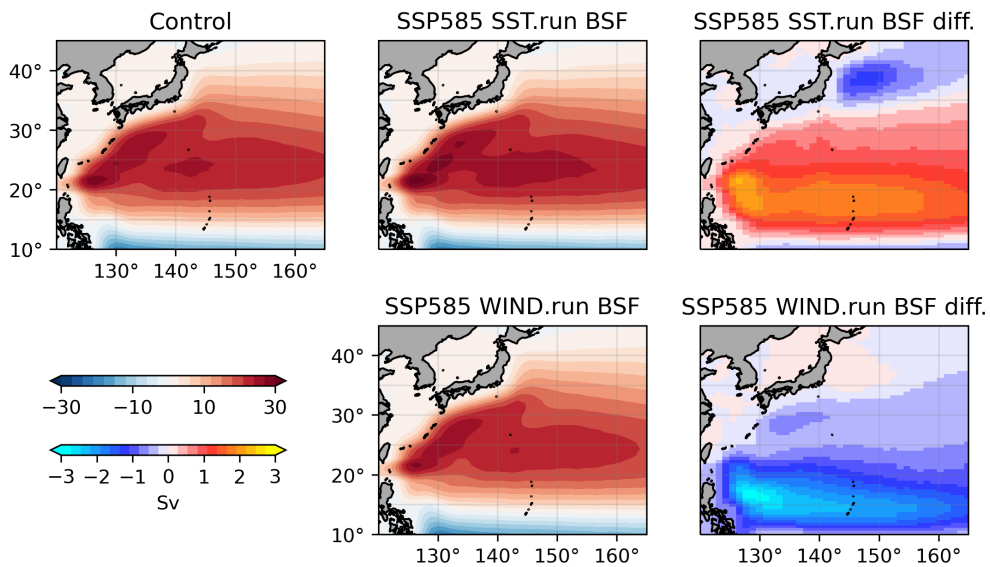

Figure A.18: The upper 300 m BSF in (a) SSP585.ctl and (b) SSP585.sst. (c) The difference between (b) SSP585.sst and (a) SSP585.ctl. (d, e) Same as (b, c) but for SSP585.wind.